

Parameter Estimation of a Gearless Pitch-Roll Wrist

PART I: Testbed Design, Modelling and Simulation

TR-CIM-10-07 September, 2010

Vikram Chopra, Xiao Qing Ma and Jorge Angeles

Centre for Intelligent Machines (CIM) &
Department of Mechanical Engineering
McGill University, Montreal (Quebec), Canada

Abstract

The work reported here pertains to the design, modelling and analysis of a testbed for a Gearless Pitch-Roll Wrist (PRW), currently under development at McGill University's Centre for Intelligent Machines. This work aims at the mechanical-parameter identification of the Spherical Epicyclic Cam Train (SECT) prototype of the PRW. The testbed is constructed and set-up, in order to conduct experiments designed to quantify mainly stiffness and damping of the PRW with the purpose of comparing its performance with that of commercial wrists. To this end, a data-acquisition system is installed and calibrated. A mathematical model of the testbed is formulated, based on which an analysis is carried out to determine that the modelled system is identifiable and controllable with its motion and torque sensors. Simulations are conducted using assumed values and are able to carefully estimate the testbed operation. Operational limits are also reported as damage to the testbed can be time-consuming and very costly to repair. Experiments and estimation of the mechanical parameters will be carried out as a second part of the project.

1 Introduction

Robotic wrists are commonly used in manipulators for applications that require a large dexterous workspace. Epicyclic bevel gear trains are commonly used in wrists, due to their relative simplicity and compactness. Rosheim (1989) developed a large survey on mechanisms commonly used in different types of robotic wrists. Tsai (1988) introduced the canonical graph of a bevel-gear robotic wrist mechanism to avoid the pseudoisomorphic problem, while providing a complete atlas of bevel-gear wrist mechanisms with up to eight links. An efficient methodology for structural synthesis of all the three degree-of-freedom (dof) robotic wrist mechanisms with N links from the catalog of two-dof geared kinematic chains with $N - 1$ links was developed by Hsu, Chang and Hsu (1999).

Researchers have made efforts to design wrists with different approaches in order to improve their performance. Wiitala and Stanisic (2000) proposed an over-constrained mechanism with a symmetric spherical eight-bar linkage, whose significant achievement is a hemisphere-singularity-free work-space. A three degree-of-freedom parallel spherical wrist was designed by Gosselin and Caron (1994), the “Agile Eye”, employing both revolute and spherical joints. Spherical Stephenson mechanisms combined with cam-rollers were proposed by Hernandez, Bai and Angeles (2006), to implement a gearless pitch-roll wrist.

The Gearless Pitch-Roll Wrist (PRW) is a system that consists of the Spherical Epicyclic Cam Train (SECT) prototype, two motors coaxially aligned with it, a data-acquisition system and a load to be manipulated. The SECT prototype, shown in Fig. 1 was designed by Bai and Angeles (2005), at the Centre for Intelligent Machines, McGill University, its role being to convert the rotations of two coaxially turning motors into one rotation coaxial with the motor rotations, the pitch, and one of axis normal to the former, the roll.

Most commonly used wrists in industrial manipulators are based on bevel-gear epicyclic trains. However, bevel-gear trains function under rolling and sliding, thereby bringing about noise and vibration. As a robotic wrist is to be attached to a moving arm, it is desirable to design such a wrist with light weight and high stiffness. Furthermore, accurate positioning

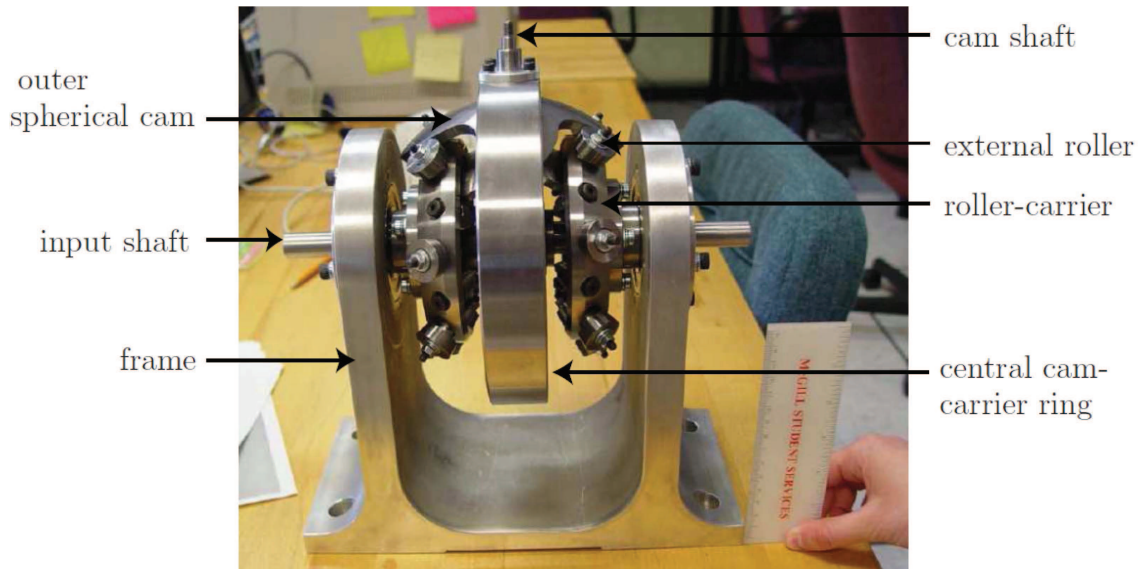


Figure 1: Spherical Epicyclic Cam Train (SECT) prototype

with low backlash is of utmost importance. The SECT takes all these factors into account to provide the advantages of high stiffness and low backlash inherent to cam-transmissions while providing an unlimited workspace.

The PRW testbed is set-up with a selection of testbed elements, as required to conduct parameter identification experiments. Torque-sensors, a data-acquisition system and couplings complement the SECT. The detailed design of the motor and torque-sensor supports along with a load, i.e., a dummy gripper¹, are reported here. The static balancing was completed in order to correctly balance the SECT with the dummy gripper. A system analysis is carried out, which includes the development of the mathematical model, its representation in state-space form and derivation of the transfer-function matrix. Simulation runs, using a MATLAB/Simulink model, are conducted.

The controllability and observability matrices are formulated and their ranks obtained. The results thereof show us that the system is both controllable and observable. Using the calculations of the gyroscopic loads in the bearings, we are able to establish the region in which we can operate the SECT within the bearing load-carrying capacity.

¹For identification purposes a functional gripper is not needed.

2 Testbed Set-up

In this section, an overview of the set-up for the Pitch-Roll Wrist testbed is discussed. The hardware and software components required to operate the SECT and to collect data are described.



Figure 2: PRW testbed

2.1 Hardware

The PRW testbed, shown in Fig. 2, and its iconic model displayed in Fig. 3, is composed of several mechanical parts and electric hardware, namely,

- four couplings: flexible shaft couplings are used in the testbed, which are connected to the servomotors, torque sensors, and the Spherical Epicyclic Cam Train (SECT).
- the SECT prototype: the prototype is to be tested here, its role being to convert the rotations of the coaxially turning motors into one rotation coaxial with the motor rotations, the pitch, and one of axis normal to the former, the roll.

- the load: we intend to use a dummy gripper that is accurately balanced with a counterweight diametrically opposed to the gripper and fixed to the central ring.
- two torque sensors: to measure the input shaft torques connected inline with the two servomotors.
- two brushless servomotors, the amplifier and the data-acquisition system, which consists of a digital/analog converter and a control platform.

Refer to Subsection 4.1 for the list of symbols used in Fig. 3.

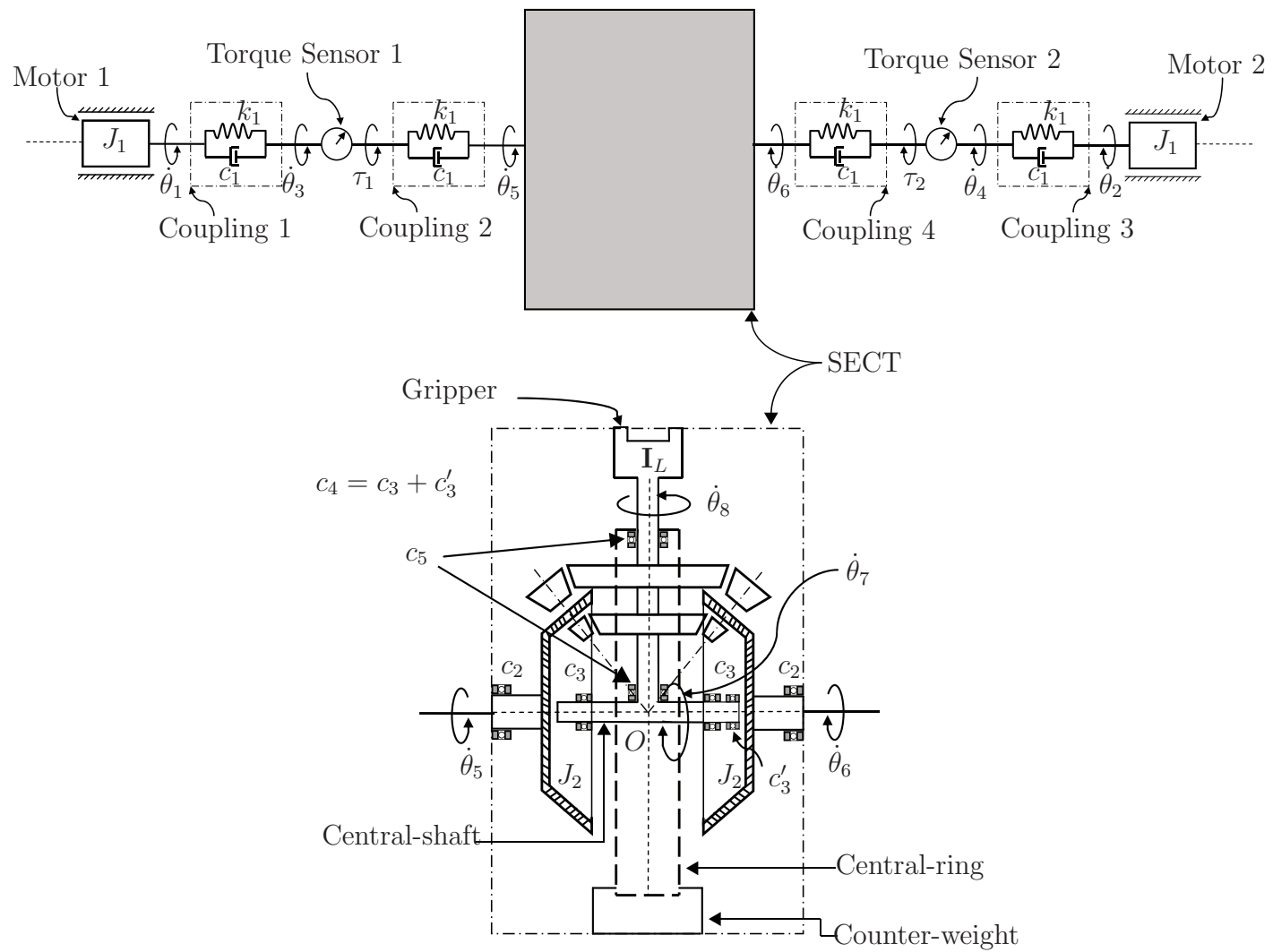


Figure 3: Iconic model of the Pitch-Roll Wrist

Table 1: Servomotor Specification

Rating	Value
Rated Power	550W
Rated Speed	2000rpm
Max. Speed	3000rpm
Cont. Stall Rating	2.68N · m
Peak Stall Torque	8.03N · m
Peak Stall Current	11.4A
Torque/Current	0.70N · m/A
Volts/1000rpm	44.6V
Rotor Inertia	$1.54 \times 10^{-5} \text{kg} \cdot \text{m} \cdot \text{s}^2$

2.1.1 Coupling Specifications

The four couplings used are DTO150B-C16-C10mm Flexible Shaft Coupling², which connect the servomotor shafts to the torque sensor shafts and the torque sensor shafts to the input shafts of the SECT. Appendix A.1 includes a figure and a detailed data sheet. Notice that the servomotor and the SECT shafts were each of 16mm of diameter, but the closest standard bore size available for the couplings is 15mm; hence, phenolic bore inserts are machined using a lathe to fit the servomotors and SECT shafts.

2.1.2 Servo Motor Specifications

We use two Glentek brushless servomotors, GMBM80550-45-0000000, to drive the SECT. Table 1 provides the specifications of the servomotors. The servomotors are to be calibrated and their parameters to be preset using an amplifier and software called MotionMAESTRO[®], which is provided by the same company. The servomotors also have encoders which provide the angular position of the shafts. Appendix A.2 includes the drawing specification.

²As per Electromate Industrial Sales Ltd. catalogue of Stocking Distributor Performance Motion Control Products, ISO 9001:2000 registered.

Available at http://www.electromate.com/products/series.php? & series_id=100287

2.1.3 Torque Sensor Specifications

For the torque measurements, we use two Futek non-contact shaft-to-shaft rotary torque sensors with encoder, FSH02055 (10 Nm capacity), to be connected coaxially in between the servomotor and SECT shafts, as shown in Fig. 2. The torque sensors, apart from measuring torques, are equipped with encoders which are capable of position measurements of the shafts. The encoders return an impulse TTL signal, where each pulse is accounted for one degree of revolution. Collecting the number of pulses over unit time gives the angular speed of the shaft. Appendix A.3 includes the specification sheet, and Fig. 4, depicts the sensors.



Figure 4: Futek torque sensor

2.1.4 Electrical Hardware

The electrical hardware set-up involves a host personal computer (PC) and input-output (I/O) devices. A PC with the operating software Windows XP[®] is used to communicate with the data-acquisition board and motor amplifier. We will use a data-acquisition system, Q8 Hardware-in-the-Loop (HIL) Control Board, supplied by Quanser Consulting Inc., which

consists of two boards; the first board, is a PCI local bus board shown in Fig. 5, is a versatile and powerful real-time measurement and control board which offers an extensive range of hardware features and software support, including MATLAB. Appendix A.4 includes the specification sheet. The second board is a terminal board which connects via ribbon cables with the PCI local bus. This is used for interfacing between the host computer and analog I/O devices.



Figure 5: Q8 hardware-in-the-loop (HIL) PCI control board

The servomotors are operated via a Glentek two axis Chassis Omega Digital amplifier, SMA9807-2A-2, as shown in Fig. 6. This amplifier is used for both controlling and calibrating the servomotor and motor-encoders. It features a built-in digital signal processor, which is capable of processing the angular displacement captured by the motor-encoders with unit time to provide measurements in angular speeds. The amplifier offers two modes of operation, namely,

- Current (Torque) Mode Servo Amplifier
- Velocity (RPM) Mode Servo Amplifier

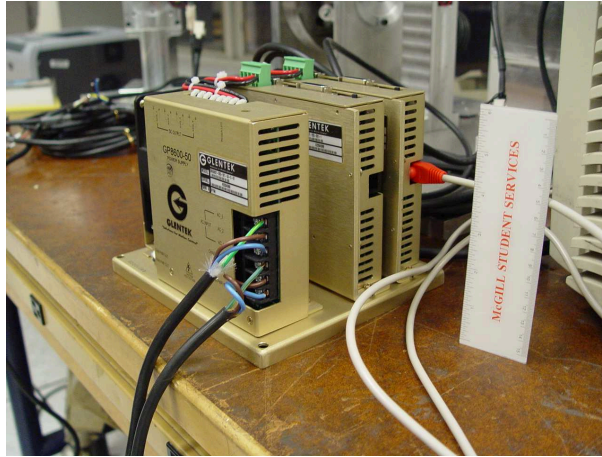


Figure 6: Glentek two-axis chassis Omega digital amplifier

2.2 Software

Quanser’s control platform is controlled by QuaRC[®], which is a multi-functional rapid control development and deployment environment, and is readily integrated with MATLAB Simulink. Control parameters may be adjusted while the code is running; thus allowing for a quick design and test iterations. The QuaRC Windows environment, shown in Fig. 7, consists of a host and target component referred to as QuaRC Host and QuaRC Target. QuaRC can communicate via the Internet, allowing the user to download controllers anywhere and control them from a remote location, change the control parameters while the controller runs, plot real-time data and save it straight into a MATLAB workspace or file.

For the servomotors and amplifier tuning purposes, we use Glentek’s MotionMAESTRO[®]. The MotionMAESTRO Windows environment, shown in Fig. 8, serves to calibrate and pre-set motor and amplifier parameters.

3 Cost Estimation

Components such as brushless servo motors, motor amplifiers, cables, torque sensors, couplings, a personal computer, data-acquisition hardware and software were bought as “off-

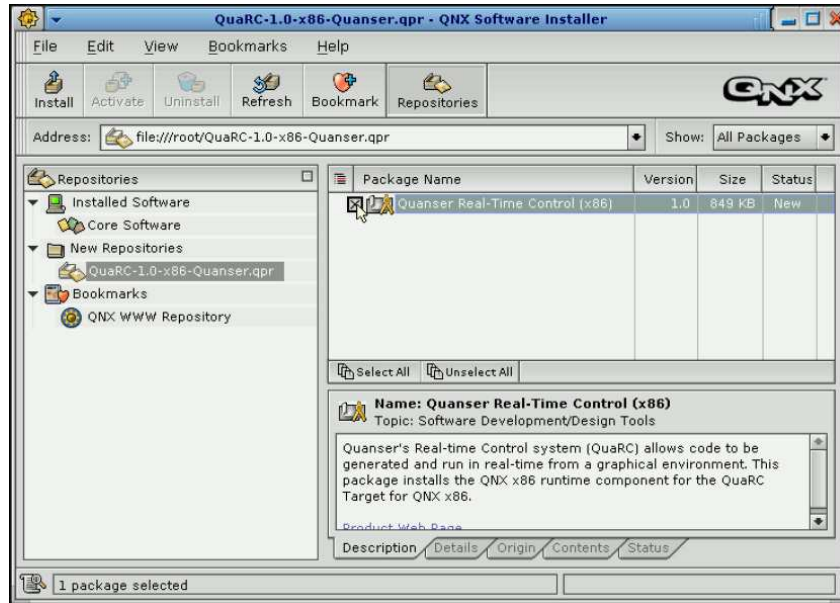


Figure 7: Quanser QuaRC®

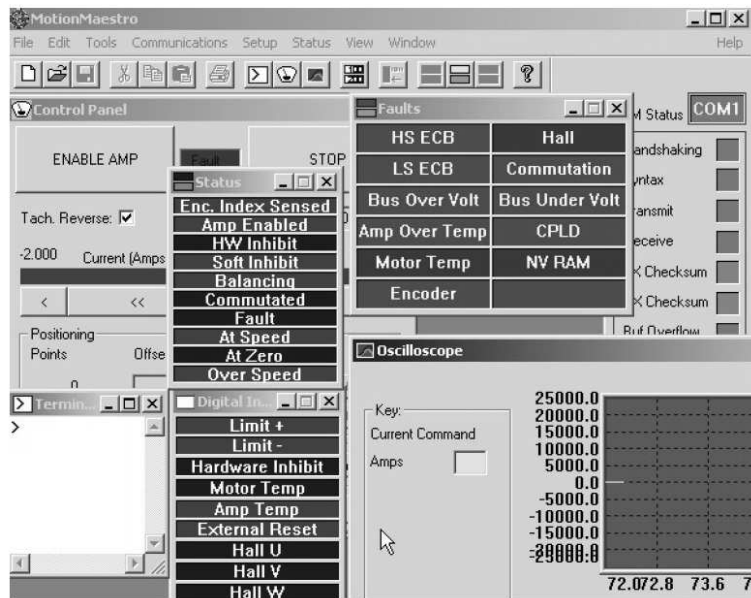


Figure 8: Glentek MotionMAESTRO®

Table 2: Cost estimation

Product	Price (\$)
Glentek brushless servo motors	1, 885.00
Glentek 2 axis chassis Omega digital amplifier	1, 945.00
Futek torque sensors	6, 270.00
Electromate couplings	340.00
Quanser Q8	4, 480.00
Quanser QuaRC	500.00
Motor support machining	1, 000.00
Torque sensor support machining	800.00
Dummy gripper machining	50.00
Counter – weightr machining	75.00
Total	17, 345.00

the-shelf” materials. Machining of the supports, gripper and counter-weight were carried out by machinist from McGill’s Machine Tool Laboratory. The SECT was machined and assembled prior to the start of this project and hence its cost are not discussed here. Listed in table 2, is a brief budgeting of the PRW testbed. Please note that prices listed do not include taxes, handling and shipping charges.

4 System Modelling

In developing the mathematical model for the testbed, we resort to a Lagrangian formulation. The transfer function of the output velocity to the input velocity is derived using the testbed iconic model of Fig. 3.

4.1 Iconic Model of the Testbed

In the iconic model of the testbed, as illustrated in Fig. 3, the shaft carrying the gripper undergoes both pitching at a rate $\dot{\theta}_7$ and rolling at $\dot{\theta}_8$. This shaft is mounted on two roller-bearings located on the central-ring. The central-shaft is rigidly coupled with the

central-ring, and this body is supported by roller-bearings located inside the roller-carriers.

4.1.1 List of Symbols describing the Iconic model of Fig. 3

k_1 : torsional stiffness of couplings 1, 2, 3 and 4

c_1 : coefficient of torsional viscous damping of couplings 1, 2, 3 and 4

c_2 : coefficient of torsional viscous damping of the roller bearings which support the input shafts of the SECT on its frame

c_3 : coefficient of torsional viscous damping of the roller bearings which support the roller-carrier on the central shaft

c'_3 : coefficient of torsional viscous damping of the roller bearings which support the central-shaft inside the roller-carrier

c_4 : equivalent coefficient of torsional viscous damping of c_3 and c'_3

c_5 : equivalent coefficient of torsional viscous damping of the two roller bearings located on the central-ring which support the cam shaft

J_1 : moment-of-inertia of motors 1 and 2

J_2 : combined moment-of-inertia of the roller-carrier, the rollers and attached input shafts

\mathbf{I}_L : combined moment-of-inertia matrix of the cam shaft, the central cam-carrier ring, gripper, counter-weight and conjugate spherical cams

$\dot{\theta}_1, \dot{\theta}_2$: angular velocities of motors 1 and 2, respectively

$\dot{\theta}_3$: angular velocity of the shaft between couplings 1 and 2

$\dot{\theta}_4$: angular velocity of the shaft between couplings 3 and 4

$\dot{\theta}_5, \dot{\theta}_6$: angular velocities of the two input shafts

$\dot{\theta}_7, \dot{\theta}_8$: rolling and pitching angular velocities of the output cam shaft

τ_1, τ_2 : torques measured by the sensors on the input shafts of the SECT

4.2 Main Assumptions

- 1 We assume that all shafts, connectors, cams and loads are rigid bodies. All bodies of the SECT are lumped in three rigid bodies, namely, the two input plates together with their rollers and attached shafts, and the combination of the central ring together with the cam shaft, central shaft, gripper and counter-weight.
- 2 The double output of the SECT prototype is a function of the two inputs, $\dot{\theta}_5$ and $\dot{\theta}_6$. The input-output relation of the SECT is given by (Bai and Angeles, 2005)

$$\begin{bmatrix} \dot{\theta}_7 \\ \dot{\theta}_8 \end{bmatrix} = \begin{bmatrix} 1/2 & 1/2 \\ N/2M & -N/2M \end{bmatrix} \begin{bmatrix} \dot{\theta}_5 \\ \dot{\theta}_6 \end{bmatrix} \quad (1)$$

where $M=4$ is the number of lobes on the spherical cams and $N=7$ is the number of rollers on each side of the roller-carrying plates of the SECT.

- 3 All springs and dashpots are torsional elements that are assumed to operate within their linear range. The elements of moments of inertia J_1 and J_2 , turning about fixed axes, as well as the central ring-cam-shaft-gripper-counterweight composite body, are also torsional elements. Notice that the latter turns about two intersecting axis, and hence, its whole 3×3 inertia matrix \mathbf{I}_L is considered.
- 4 The composite body of the cam-shaft-gripper-counterweight-ring is assumed to be statically balanced, as its balancing was a design task described in Appendix B.3, with its centre of mass located at the intersection O of the axes of pitching and rolling.

4.3 Formation of the Mathematical Model

We proceed to formulate the governing equations of the mechanical system at hand. Let \mathbf{q} be the vector of independent generalized coordinates; then, the Lagrange equation of the

system is derived using the formulation proposed by Angeles (2008), namely,

$$\frac{d}{dt} \left(\frac{\partial L}{\partial \dot{\mathbf{q}}} \right) - \frac{\partial L}{\partial \mathbf{q}} = \frac{\partial(\Pi - \Delta)}{\partial \dot{\mathbf{q}}} \quad (2)$$

where

L : the Lagrangian of the system, given by $L = T - V$

T : the total kinetic energy of the system

V : the total potential energy of the system

Π : the power supplied to the system by force sources

Δ : the Rayleigh dissipation function associated with all the dashpots in the system

\mathbf{q} : the six-dimensional vector of angular displacements θ_i , for $i = 3, 4, \dots, 8$

Note, that the two angular velocities $\dot{\theta}_1$ and $\dot{\theta}_2$ of the two motors are specified, which play the role of control variables and hence, are not generalized coordinates. As well, given that the system is motion-driven, the power Π supplied by force sources vanishes, i.e.,

$$\Pi = 0 \quad (3)$$

4.3.1 Kinetic Energy

The total kinetic energy is determined as the sum of all the individual kinetic energies of the different components in the system, namely,

$$T = \frac{1}{2}J_1\dot{\theta}_1^2 + \frac{1}{2}J_1\dot{\theta}_2^2 + \frac{1}{2}J_2\dot{\theta}_5^2 + \frac{1}{2}J_2\dot{\theta}_6^2 + \frac{1}{2}\boldsymbol{\omega}_L^T \mathbf{I}_L \boldsymbol{\omega}_L \quad (4)$$

Notice that the 3×3 inertia matrix \mathbf{I}_L is constant when referred to a moving frame, with origin at O , X -axis defined as the axis of pitching, Y -axis as the axis of rolling, and Z -axis forming a right-hand frame with X and Y . In this frame, by virtue of the geometric

symmetry of the composite body at stake, moreover, \mathbf{I}_L is diagonal, and hence,

$$\mathbf{I}_L = \begin{bmatrix} H_3 & 0 & 0 \\ 0 & J_3 & 0 \\ 0 & 0 & K_3 \end{bmatrix}, \quad \boldsymbol{\omega}_L = \begin{bmatrix} \dot{\theta}_7 \\ \dot{\theta}_8 \\ 0 \end{bmatrix} \quad (5a)$$

whence,

$$\frac{1}{2} \boldsymbol{\omega}_L^T \mathbf{I}_L \boldsymbol{\omega}_L = \frac{1}{2} H_3 \dot{\theta}_7^2 + \frac{1}{2} J_3 \dot{\theta}_8^2 \quad (5b)$$

Substituting eq.(5b) in eq.(4) yields

$$T = \frac{1}{2} J_1 \dot{\theta}_1^2 + \frac{1}{2} J_1 \dot{\theta}_2^2 + \frac{1}{2} J_2 \dot{\theta}_5^2 + \frac{1}{2} J_2 \dot{\theta}_6^2 + \frac{1}{2} H_3 \dot{\theta}_7^2 + \frac{1}{2} J_3 \dot{\theta}_8^2 \quad (6)$$

4.3.2 Potential Energy

The total potential energy is determined by the elastic elements, while gravity does not intervene, as per Assumption 4.2. Hence,

$$V = \frac{1}{2} k_1 (\theta_1 - \theta_3)^2 + \frac{1}{2} k_1 (\theta_2 - \theta_4)^2 + \frac{1}{2} k_1 (\theta_3 - \theta_5)^2 + \frac{1}{2} k_1 (\theta_4 - \theta_6)^2 \quad (7)$$

4.3.3 Dissipation Function

The Rayleigh dissipation function associated with the system stems from the viscous damping present, which is

$$\begin{aligned} \Delta = & \frac{1}{2} c_1 (\dot{\theta}_1 - \dot{\theta}_3)^2 + \frac{1}{2} c_1 (\dot{\theta}_2 - \dot{\theta}_4)^2 + \frac{1}{2} c_1 (\dot{\theta}_3 - \dot{\theta}_5)^2 + \frac{1}{2} c_1 (\dot{\theta}_4 - \dot{\theta}_6)^2 \\ & + \frac{1}{2} c_2 \dot{\theta}_5^2 + \frac{1}{2} c_2 \dot{\theta}_6^2 + \frac{1}{2} c_3 (\dot{\theta}_5 - \dot{\theta}_7)^2 + \frac{1}{2} c_4 (\dot{\theta}_6 - \dot{\theta}_7)^2 + \frac{1}{2} c_5 \dot{\theta}_8^2 \end{aligned} \quad (8)$$

4.3.4 Equation of Motion

We have a system with six degrees with freedom, θ_i , for $i = 3, 4, \dots, 8$, denoting the generalized coordinates. Now, integrating the input-output relation of eq.(1), with respect to time,

under the assumption that at initial conditions (i.e., at $t = 0$) all terms vanish, we notice that out of the six generalized coordinates only four are independent. Hence, the system has, in fact, four degrees of freedom. Under these conditions, we substitute eqs.(6)–(8) into eq.(2), the Lagrange equation then leading to

$$\mathbf{M}\ddot{\mathbf{q}} + \mathbf{\Delta}\dot{\mathbf{q}} + \mathbf{K}\mathbf{q} = \mathbf{f}(t) \quad (9)$$

where \mathbf{q} is the four-dimensional vector of generalized coordinates and $\mathbf{f}(t)$ is the four-dimensional vector of input generalized force, namely,

$$\mathbf{q} = \begin{bmatrix} \theta_3 \\ \theta_4 \\ \theta_5 \\ \theta_6 \end{bmatrix}, \quad \mathbf{f}(t) = \begin{bmatrix} c_1\dot{\theta}_1 + k_1\theta_1 \\ c_1\dot{\theta}_2 + k_1\theta_2 \\ 0 \\ 0 \end{bmatrix}$$

Furthermore, \mathbf{M} , \mathbf{C} and \mathbf{K} are the 4×4 mass, damping and stiffness matrices, respectively, namely,

$$\mathbf{M} = \begin{bmatrix} 0 & 0 & 0 & 0 \\ 0 & 0 & 0 & 0 \\ 0 & 0 & (J_2 + H_3/4 + J_3N^2/4M^2) & (H_3/4 - J_3N^2/4M^2) \\ 0 & 0 & (H_3/4 - J_3N^2/4M^2) & (J_2 + H_3/4 + J_3N^2/4M^2) \end{bmatrix}$$

$$\mathbf{\Delta} = \begin{bmatrix} 2c_1 & 0 & -c_1 & 0 \\ 0 & 2c_1 & 0 & -c_1 \\ -c_1 & 0 & (c_1 + c_2 + c_3/4 + c_4/4 + c_5N^2/4M^2) & (-c_3/4 - c_4/4 - c_5N^2/4M^2) \\ 0 & -c_1 & (-c_3/4 - c_4/4 - c_5N^2/4M^2) & (c_1 + c_2 + c_3/4 + c_4/4 + c_5N^2/4M^2) \end{bmatrix}$$

$$\mathbf{K} = \begin{bmatrix} 2k_1 & 0 & -k_1 & 0 \\ 0 & 2k_1 & 0 & -k_1 \\ -k_1 & 0 & k_1 & 0 \\ 0 & -k_1 & 0 & k_1 \end{bmatrix}$$

4.4 State-Space Representation

A state-space representation as a multiple-input-multiple-output system (MIMO) is derived below. This is needed in order to derive the system transfer functions, which will be used, in turn, to identify the system model parameters. In order to represent the mathematical model in state-space, we first reduce the model given by eq.(9) to a two-dimensional second-order definite system coupled with a two-dimensional first-order system. To this end, matrices and vectors are partitioned as,

$$\mathbf{M} = \begin{bmatrix} \mathbf{O} & \mathbf{O} \\ \mathbf{O} & \mathbf{M}_{II} \end{bmatrix}, \quad \Delta = \begin{bmatrix} \mathbf{C}_I & \mathbf{C}_{I,II} \\ \mathbf{C}_{I,II}^T & \mathbf{C}_{II} \end{bmatrix}, \quad \mathbf{K} = \begin{bmatrix} \mathbf{K}_I & \mathbf{K}_{I,II} \\ \mathbf{K}_{I,II}^T & \mathbf{K}_{II} \end{bmatrix}$$

$$\mathbf{q} = \begin{bmatrix} \mathbf{q}_I \\ \mathbf{q}_{II} \end{bmatrix}, \quad \mathbf{q}_I = \begin{bmatrix} \theta_3 \\ \theta_4 \end{bmatrix}, \quad \mathbf{q}_{II} = \begin{bmatrix} \theta_5 \\ \theta_6 \end{bmatrix}$$

$$\mathbf{f}(t) = \begin{bmatrix} \mathbf{f}_I \\ \mathbf{0} \end{bmatrix}, \quad \mathbf{f}_I = \mathbf{F}\mathbf{u}, \quad \mathbf{F} = [\mathbf{K}_{1,in} \quad \mathbf{C}_{1,in}], \quad \mathbf{K}_{1,in} = \begin{bmatrix} k_1 & 0 \\ 0 & k_1 \end{bmatrix}$$

$$\mathbf{C}_{1,in} = \begin{bmatrix} c_1 & 0 \\ 0 & c_1 \end{bmatrix}, \quad \mathbf{u} = \begin{bmatrix} \boldsymbol{\theta}_{in} \\ \boldsymbol{\omega}_{in} \end{bmatrix}, \quad \boldsymbol{\omega}_{in} = \begin{bmatrix} \dot{\theta}_1 \\ \dot{\theta}_2 \end{bmatrix}, \quad \boldsymbol{\theta}_{in} = \int_0^t \boldsymbol{\omega}(\lambda) d\lambda$$

where we define $\mathbf{0}$ as the two-dimensional zero vector, \mathbf{O} as the 2×2 zero matrix, all blocks being of 2×2 . Then, the mathematical model takes the form

$$\mathbf{C}_I \dot{\mathbf{q}}_I + \mathbf{C}_{I,II} \dot{\mathbf{q}}_{II} + \mathbf{K}_I \mathbf{q}_I + \mathbf{K}_{I,II} \mathbf{q}_{II} = \mathbf{F}\mathbf{u} \quad (10a)$$

$$\mathbf{M}_{II} \ddot{\mathbf{q}}_{II} + \mathbf{C}_{I,II}^T \dot{\mathbf{q}}_I + \mathbf{C}_{II} \dot{\mathbf{q}}_{II} + \mathbf{K}_{I,II}^T \mathbf{q}_I + \mathbf{K}_{II} \mathbf{q}_{II} = \mathbf{0} \quad (10b)$$

Further, let $\dot{\mathbf{q}}_J = \mathbf{v}_J$, for $J = I, II$. Then,

$$\dot{\mathbf{q}}_I = \mathbf{v}_I = \mathbf{C}_I^{-1}(\mathbf{F}\mathbf{u} - \mathbf{C}_{I,II}\mathbf{v}_{II} - \mathbf{K}_I \mathbf{q}_I - \mathbf{K}_{I,II} \mathbf{q}_{II}) \quad (11a)$$

$$\dot{\mathbf{q}}_{II} = \mathbf{v}_{II} \quad (11b)$$

$$\dot{\mathbf{v}}_{II} = -\mathbf{M}_{II}^{-1}(\mathbf{C}_{I,II}^T \mathbf{v}_I + \mathbf{C}_{II} \mathbf{v}_{II} + \mathbf{K}_{I,II}^T \mathbf{q}_I + \mathbf{K}_{II} \mathbf{q}_{II})$$

Substituting eq.(11a) into the third equation of the above set,

$$\begin{aligned} \dot{\mathbf{v}}_{II} = & -\mathbf{M}_{II}^{-1}[\mathbf{C}_{I,II}^T \mathbf{C}_I^{-1}(\mathbf{F}\mathbf{u} - \mathbf{C}_{I,II}\mathbf{v}_{II} - \mathbf{K}_I\mathbf{q}_I - \mathbf{K}_{I,II}\mathbf{q}_{II}) + \mathbf{C}_{II}\mathbf{v}_{II} \\ & + \mathbf{K}_{I,II}^T\mathbf{q}_I + \mathbf{K}_{II}\mathbf{q}_{II}] \end{aligned} \quad (11c)$$

Therefore, we have six state-variable equations. Regarding the system output, we have sensors to measure torque and angular speeds. The motor-encoders measure actual values for $\boldsymbol{\omega}_{in}$ while torque-sensors with encoders provide measurements for $\dot{\mathbf{q}}_I$, τ_1 and τ_2 . The free-body diagram of coupling 1 is shown in Fig. 9. As the body inside the dashed box is massless, its equilibrium yields

$$\tau_1 = k_1(\theta_3 - \theta_1) + c_1(\dot{\theta}_3 - \dot{\theta}_1) \quad (12)$$

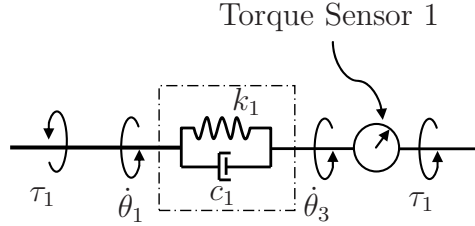


Figure 9: Coupling 1 of the PRW

Similarly, for coupling 3,

$$\tau_2 = k_1(\theta_4 - \theta_2) + c_1(\dot{\theta}_4 - \dot{\theta}_2) \quad (13)$$

Thus,

$$\boldsymbol{\gamma} = \begin{bmatrix} \tau_1 \\ \tau_2 \end{bmatrix} = \begin{bmatrix} k_1 & 0 \\ 0 & k_1 \end{bmatrix} \mathbf{q}_I + \begin{bmatrix} c_1 & 0 \\ 0 & c_1 \end{bmatrix} \dot{\mathbf{q}}_I - \mathbf{F}\mathbf{u} \quad (14)$$

and hence,

$$\boldsymbol{\gamma} = \mathbf{K}_{1,in}\mathbf{q}_I + \mathbf{C}_{1,in}\dot{\mathbf{q}}_I - \mathbf{F}\mathbf{u} \quad (15)$$

Upon rearranging the terms in eq.(15) and substituting $\dot{\mathbf{q}}_I$ from eq.(11a) in it, one obtains

$$\begin{aligned} \gamma = & (\mathbf{K}_{1,in} - \mathbf{C}_{1,in} \mathbf{C}_I^{-1} \mathbf{K}_I) \mathbf{q}_I - \mathbf{C}_{1,in} \mathbf{C}_I^{-1} \mathbf{K}_{I,II} \mathbf{q}_{II} - \mathbf{C}_{1,in} \mathbf{C}_I^{-1} \mathbf{C}_{I,II} \mathbf{v}_{II} \\ & - (\mathbf{C}_{1,in} \mathbf{C}_I^{-1} - \mathbf{1}) \mathbf{F} \mathbf{u} \end{aligned} \quad (16)$$

thereby deriving, an expression for the measured torques. Proceeding with the state-space representation, let the state-variable vector \mathbf{x} and the output-variable vector \mathbf{y} be defined as

$$\mathbf{x} = [\mathbf{q}_I, \mathbf{q}_{II}, \mathbf{v}_{II}]^T \quad \mathbf{y} = [\dot{\mathbf{q}}_I, \boldsymbol{\omega}_{in}, \boldsymbol{\gamma}]^T$$

Then the state-space model takes the form,

$$\dot{\mathbf{x}} = \mathbf{A} \mathbf{x} + \mathbf{B} \mathbf{u} \quad (17a)$$

$$\mathbf{y} = \mathbf{C} \mathbf{x} + \mathbf{D} \mathbf{u} \quad (17b)$$

where

$$\begin{aligned} \mathbf{A} &= \begin{bmatrix} \mathbf{A}_{11} & \mathbf{A}_{12} & \mathbf{A}_{13} \\ \mathbf{O} & \mathbf{O} & \mathbf{1} \\ \mathbf{A}_{31} & \mathbf{A}_{32} & \mathbf{A}_{33} \end{bmatrix}, \quad \mathbf{B} = \begin{bmatrix} \mathbf{B}_{11} & \mathbf{B}_{12} \\ \mathbf{O} & \mathbf{O} \\ \mathbf{B}_{31} & \mathbf{B}_{32} \end{bmatrix} \\ \mathbf{C} &= \begin{bmatrix} \mathbf{O} & \mathbf{O} & \mathbf{O} \\ \mathbf{O} & \mathbf{O} & \mathbf{O} \\ \mathbf{C}_{31} & \mathbf{C}_{32} & \mathbf{C}_{33} \end{bmatrix}, \quad \mathbf{D} = \begin{bmatrix} \mathbf{O} & \mathbf{O} \\ \mathbf{O} & \mathbf{1} \\ \mathbf{D}_{31} & \mathbf{D}_{32} \end{bmatrix} \end{aligned}$$

with

$$\mathbf{A}_{11} = \mathbf{C}_I^{-1} \mathbf{K}_I$$

$$\mathbf{A}_{12} = \mathbf{C}_I^{-1} \mathbf{K}_{I,II}$$

$$\mathbf{A}_{13} = \mathbf{C}_I^{-1} \mathbf{C}_{I,II}$$

$$\mathbf{A}_{31} = -\mathbf{M}_{II}^{-1} (-\mathbf{C}_{I,II}^T \mathbf{C}_I^{-1} \mathbf{K}_I + \mathbf{K}_{I,II}^T)$$

$$\mathbf{A}_{32} = -\mathbf{M}_{II}^{-1} (-\mathbf{C}_{I,II}^T \mathbf{C}_I^{-1} \mathbf{K}_{I,II} + \mathbf{K}_{II})$$

$$\begin{aligned}
\mathbf{A}_{33} &= -\mathbf{M}_{II}^{-1}(-\mathbf{C}_{I,II}^T \mathbf{C}_I^{-1} \mathbf{C}_{I,II} + \mathbf{C}_{II}) \\
\mathbf{B}_{11} &= \mathbf{C}_I^{-1} \mathbf{K}_{1,in} \\
\mathbf{B}_{12} &= \mathbf{C}_I^{-1} \mathbf{C}_{1,in} \\
\mathbf{B}_{31} &= -\mathbf{M}_{II}^{-1} \mathbf{C}_{I,II}^T \mathbf{C}_I^{-1} \mathbf{K}_{1,in} \\
\mathbf{B}_{32} &= -\mathbf{M}_{II}^{-1} \mathbf{C}_{I,II}^T \mathbf{C}_I^{-1} \mathbf{C}_{1,in} \\
\mathbf{C}_{31} &= \mathbf{K}_{1,in} - \mathbf{C}_{1,in} \mathbf{C}_I^{-1} \mathbf{K}_I \\
\mathbf{C}_{32} &= -\mathbf{C}_{1,in} \mathbf{C}_I^{-1} \mathbf{K}_{I,II} \\
\mathbf{C}_{33} &= -\mathbf{C}_{1,in} \mathbf{C}_I^{-1} \mathbf{C}_{I,II} \\
\mathbf{D}_{31} &= -\mathbf{C}_{1,in} \mathbf{C}_I^{-1} \mathbf{K}_{1,in} - \mathbf{K}_{1,in} \\
\mathbf{D}_{32} &= -\mathbf{C}_{1,in} \mathbf{C}_I^{-1} \mathbf{C}_{1,in} - \mathbf{C}_{1,in}
\end{aligned}$$

and $\mathbf{1}$ is the 2×2 identity matrix.

4.5 Derivation of the Transfer Function

With the state-space representation complete, the transfer function is derived in order to describe the ratios of the output variables to the input variables. We take the Laplace transforms of eqs.(17a) and (17b), to obtain

$$s\mathbf{X}(s) = \mathbf{A}\mathbf{X}(s) + \mathbf{B}U(s) \quad (18a)$$

$$\mathbf{Y}(s) = \mathbf{C}\mathbf{X}(s) + \mathbf{D}U(s) \quad (18b)$$

where $U(s)$, $\mathbf{X}(s)$ and $\mathbf{Y}(s)$ denote the Laplace transforms of vectors $\mathbf{u}(t)$, $\mathbf{x}(t)$ and $\mathbf{y}(t)$, respectively. Therefore,

$$\mathbf{X}(s) = (s\mathbf{1} - \mathbf{A})^{-1} \mathbf{B}U(s) \quad (19)$$

$$\mathbf{Y}(s) = [\mathbf{C}(s\mathbf{1} - \mathbf{A})^{-1} \mathbf{B}]U(s) + \mathbf{D}U(s) \quad (20)$$

Table 3: Inertial Properties

Component	Mass (kg)	Moment of Inertia (kg · m ²)			
rollers-plate-shaft	2.16	3.87×10^{-3}			
ring-cam-shaft-gripper-counter	6.09	4.22	0	0	$\times 10^{-2}$
		0	1.33	0	
		0	0	3.21	

Thus, the transfer function $\mathbf{G}(s)$ is obtained as

$$\mathbf{G}(s) \equiv \frac{\partial \mathbf{Y}(s)}{\partial \mathbf{U}(s)} = \mathbf{C}(s\mathbf{1} - \mathbf{A})^{-1}\mathbf{B} + \mathbf{D} \quad (21)$$

where \mathbf{A} , \mathbf{B} , \mathbf{C} and \mathbf{D} are given in eqs.(17a) and (17b), matrix $\mathbf{G}(s)$ thus being of 6×4 , and hence yielding 24 transfer functions. Given that two components of vector \mathbf{u} are the time-integrals of the other two, their scalar transfer functions cannot be independent. The transfer-function matrix can thus be reduced to one of 6×2 by properly expressing the Laplace transform of θ_{in} as $\Omega_{in}(s)/s$, where $\Omega_{in}(s)$ is $\mathcal{L}\{\omega_{in}(t)\}$.

4.6 Inertial Properties of the SECT

In order to conduct simulation and analysis of the PRW testbed, the inertial properties of the SECT are required. For the given model, we require the mass and moment of inertia of the roller-plate-shaft composite body, and the cam-shaft-griper-ring composite body. To this end, we resort to a CAD software package, namely, Pro/ENGINEER, where the SECT was previously generated. This software package includes a useful tool called Model Analysis, which is used to calculate volumetric properties of solid elements. Table 3 displays the inertial properties calculated with Pro/ENGINEER.

4.7 Gyroscopic Loads in the SECT Bearings

We estimate the gyroscopic loads on the SECT bearings in this subsection. This is an important issue because it determines the limits for operation during tests. It is crucial to outline the operational speeds as loads induced by gyroscopic moments are capable of damaging the bearings of the SECT, which can be expensive to replace and time-consuming. Let \mathbf{h} represent the angular momentum of the composite body ring-cam-shaft-gripper from eq.(5a); we have

$$\mathbf{h} = \mathbf{I}_L \boldsymbol{\omega}_L = \begin{bmatrix} H_3 \dot{\theta}_7 \\ J_3 \dot{\theta}_8 \\ 0 \end{bmatrix} \quad (22)$$

Then the rate of change of the angular momentum, under the assumption that $\dot{\theta}_7$ and $\dot{\theta}_8$ are constant, is

$$\dot{\mathbf{h}} = \boldsymbol{\omega}_L \times \mathbf{I}_L \boldsymbol{\omega}_L \quad (23)$$

which yields

$$\dot{\mathbf{h}} = \mathbf{k} \dot{\theta}_7 \dot{\theta}_8 (J_3 - H_3) \quad (24)$$

where \mathbf{k} is the unit vector parallel to the axis of the cam-shaft, as described in Subsection 4.3.1.

Notice that the largest ball bearings are present on the support housing of the SECT, as shown in Fig. 10. We perform a static force analysis on the SECT; upon assuming symmetry, the radial force in the bearings F_b is given by

$$F_b = \frac{J_3 - H_3}{2\ell} \dot{\theta}_7 \dot{\theta}_8 \quad (25)$$

where ℓ is the distance between the cam-carrying shaft axis and the centre of the ball bearing, a SKF-6306.

Using the bearing data sheet³ supplied by the manufacturer (see Appendix A.5), which

³Available from the SKF online catalog at <http://www.skf.com/skf/productcatalogue/Forwarder?>

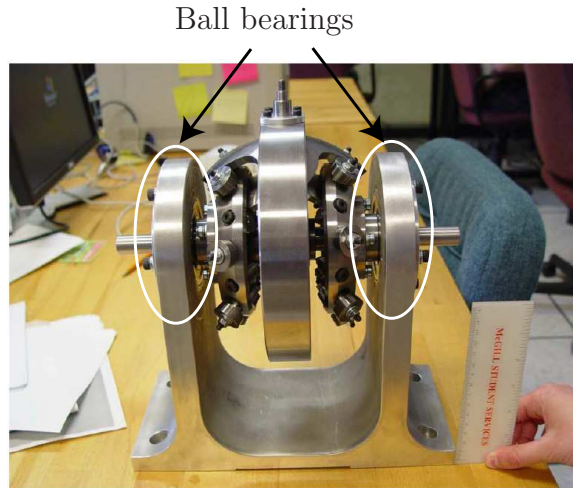


Figure 10: Largest sized ball bearings (SKF-6306) present in the SECT

shows a maximum static load rating of 16kN, we equate this value with the right-hand side of eq.(25) and plot a graph using Maple. The shaded region, shown in Fig. 11, is the allowable operation region.

5 Simulation of the Testbed

We recreate the testbed model in MATLAB in order to conduct simulations. We begin by assuming some values for the system parameters. These are obtained from previous work done on the design of a testbed for a novel speed reducer, namely, the spherical Speed-o-Cam prototype. Stiffness and damping identifications were experimentally done of this prototype and of the testbed couplings. We assume for simulation purposes that the stiffness and damping parameters are similar to those of the Speed-o-Cam testbed, as listed in Table 4. Moreover, the damping present in the bearings of the SECT as estimated to be about $\pm 15\%$ (Song, 2002).

Using the parameters from the Table 4, we conduct the simulation runs in MATLAB.

With reference to the iconic model of Fig. 3 and its list of symbols, we construct a MAT-

action=PPP & lang=en & imperial=false & windowName=null & perfid=105001 & prodid=1050010306

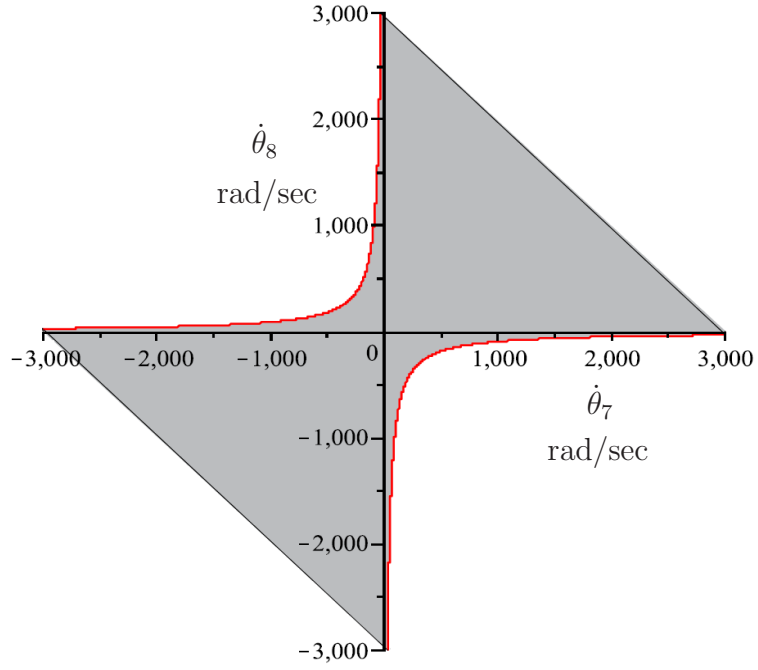


Figure 11: Allowable operation region at constant rpm

Table 4: Simulation Parameters

Parameter	Value
J_2	$3.87 \times 10^{-3} \text{kg} \cdot \text{m}^2$
H_3	$4.22 \times 10^{-2} \text{kg} \cdot \text{m}^2$
J_3	$1.33 \times 10^{-2} \text{kg} \cdot \text{m}^2$
c_1	$7.83 \times 10^{-3} \text{N} \cdot \text{m} \cdot \text{s}/\text{deg}$
c_2	$8.35 \times 10^{-3} \text{N} \cdot \text{m} \cdot \text{s}/\text{deg}$
c_3	$9.00 \times 10^{-3} \text{N} \cdot \text{m} \cdot \text{s}/\text{deg}$
c_4	$6.66 \times 10^{-3} \text{N} \cdot \text{m} \cdot \text{s}/\text{deg}$
c_5	$7.10 \times 10^{-3} \text{N} \cdot \text{m} \cdot \text{s}/\text{deg}$
k_1	$2.11 \text{N} \cdot \text{m}/\text{deg}$
M	4
N	7

LAB Simulink control system model, as shown in Figs. 12 & 13. The programming codes to operate this Simulink model is written in MATLAB itself (as a M-file). Included in Appendix C is a sample M-file piece of code.

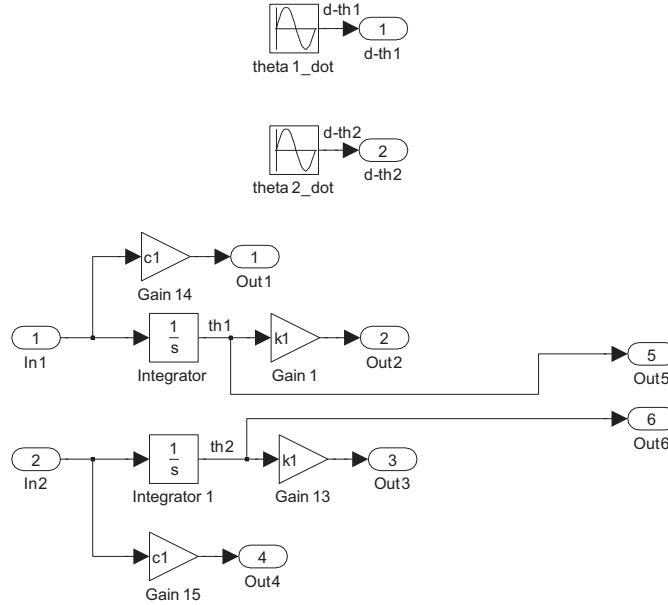


Figure 12: MATLAB Simulink model for the two inputs

5.1 Simulation Results

Simulation runs using frequencies of 1Hz, 10Hz, 50Hz and 1000Hz are carried out. Beginning with a frequency of 1Hz, we test our Simulink model using the same amplitude but phase differences of both 0° and 180° . Notice that in the former case, we only achieve pitch motion and negligible disturbance in the rolling motion, as shown on the respective scopes in Figs.14–16. Similarly, in the latter case as shown in Figs. 17–19, only rolling motion is achieved with a negligible disturbance (in the form of beating) in the pitch motion. For the other frequencies, a phase difference of 180° and different amplitudes (by setting one input amplitude to be half of the other). Shown in Figs. 20–28 are the respective simulation scopes.

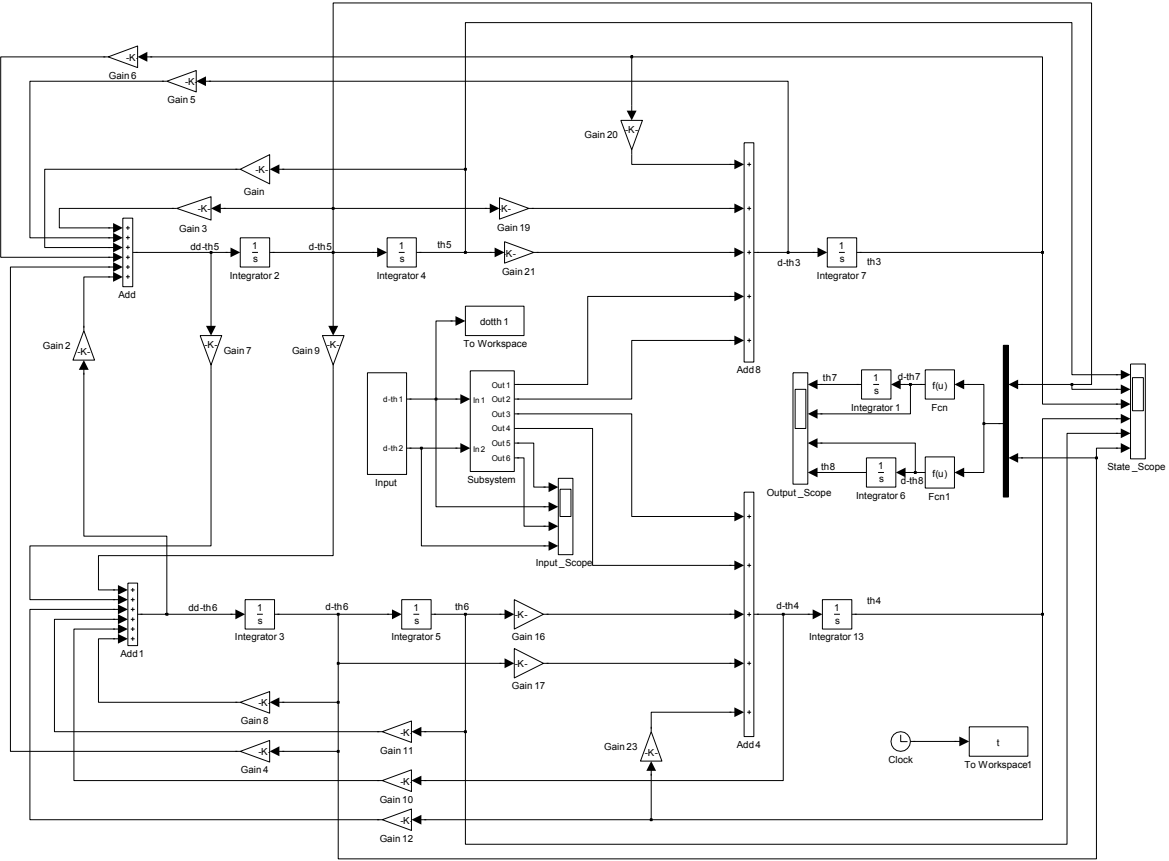


Figure 13: MATLAB Simulink system model

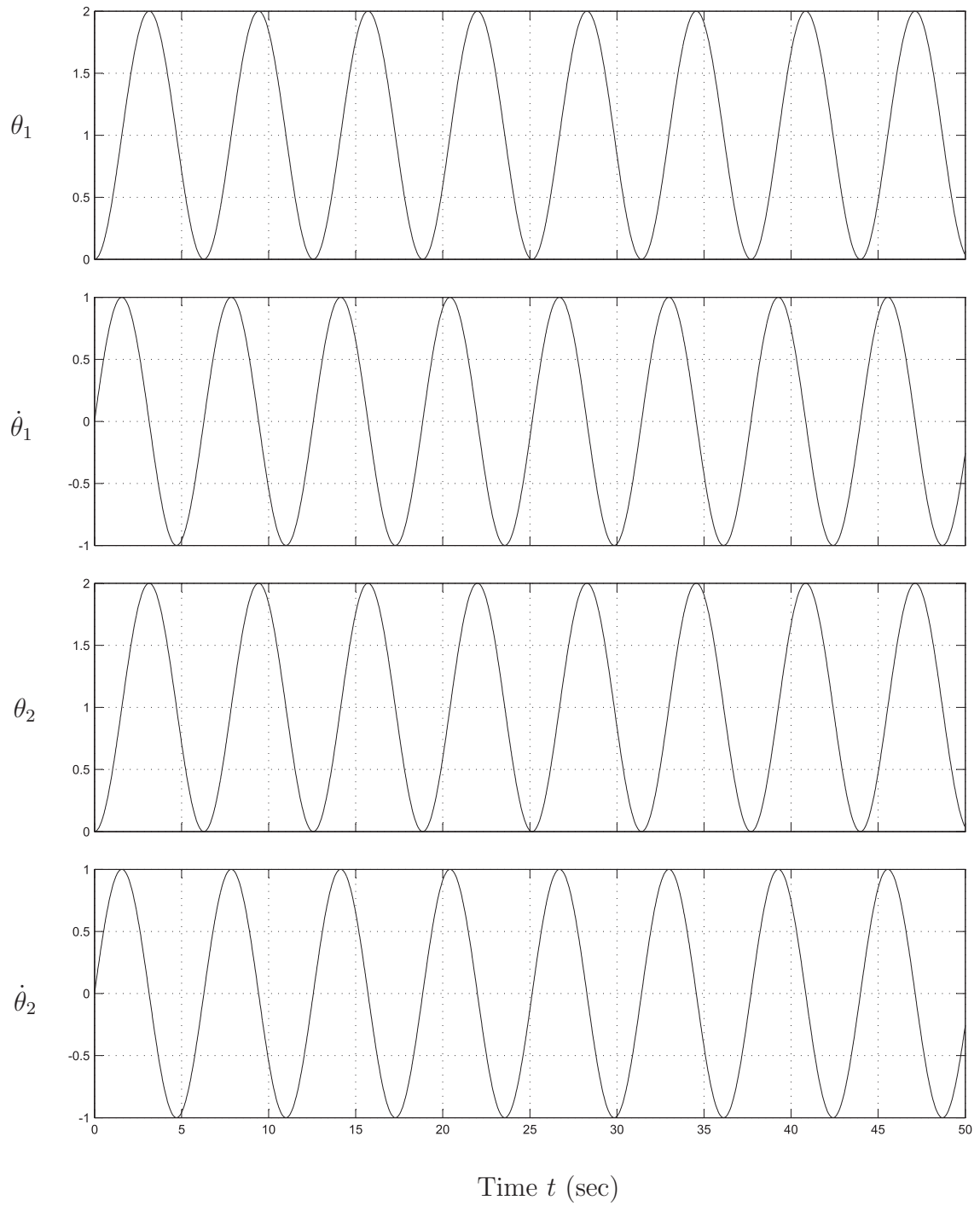


Figure 14: 1Hz (Same amplitude, phase difference 0°) input scope

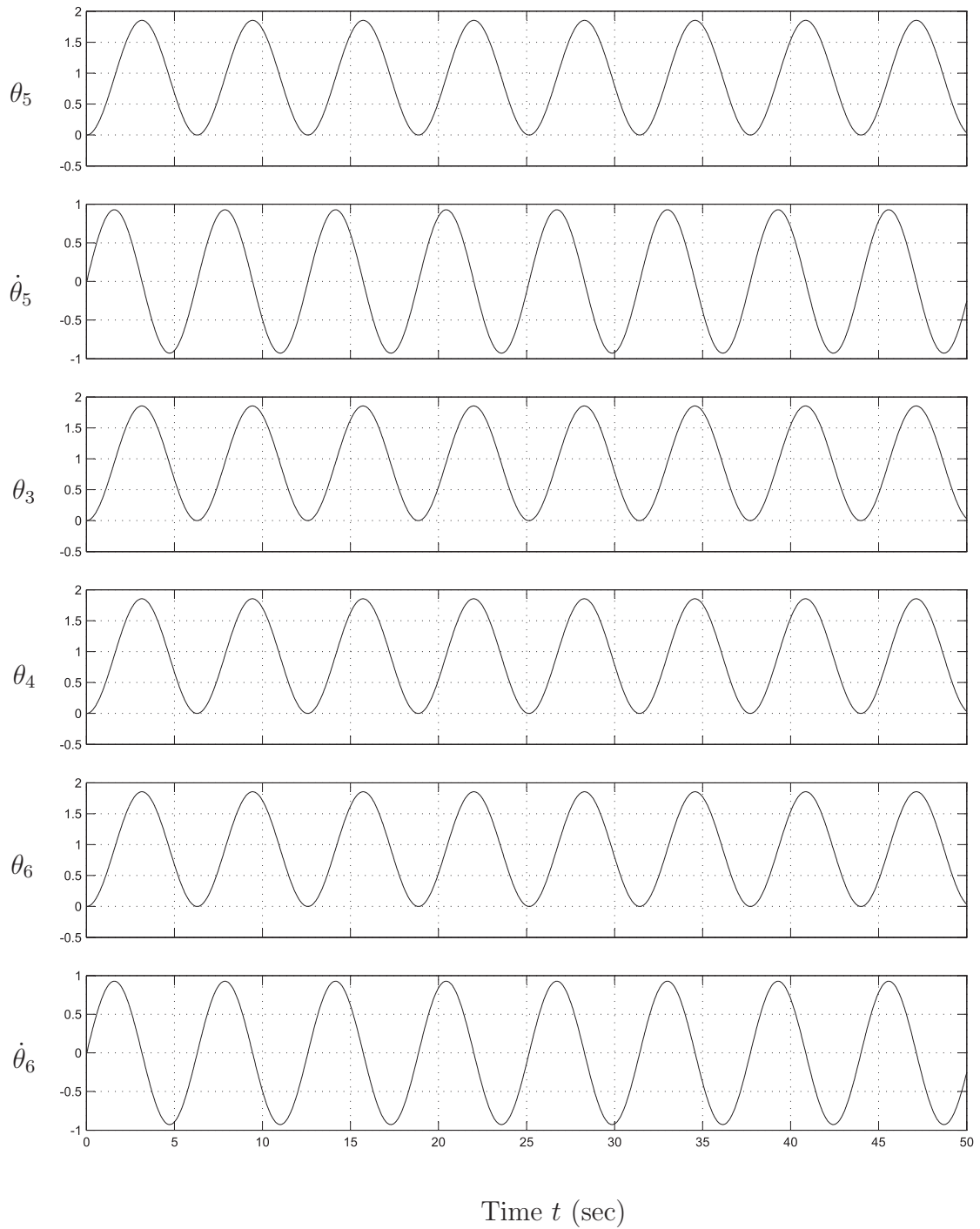


Figure 15: 1Hz (Same amplitude, phase difference 0°) state scope

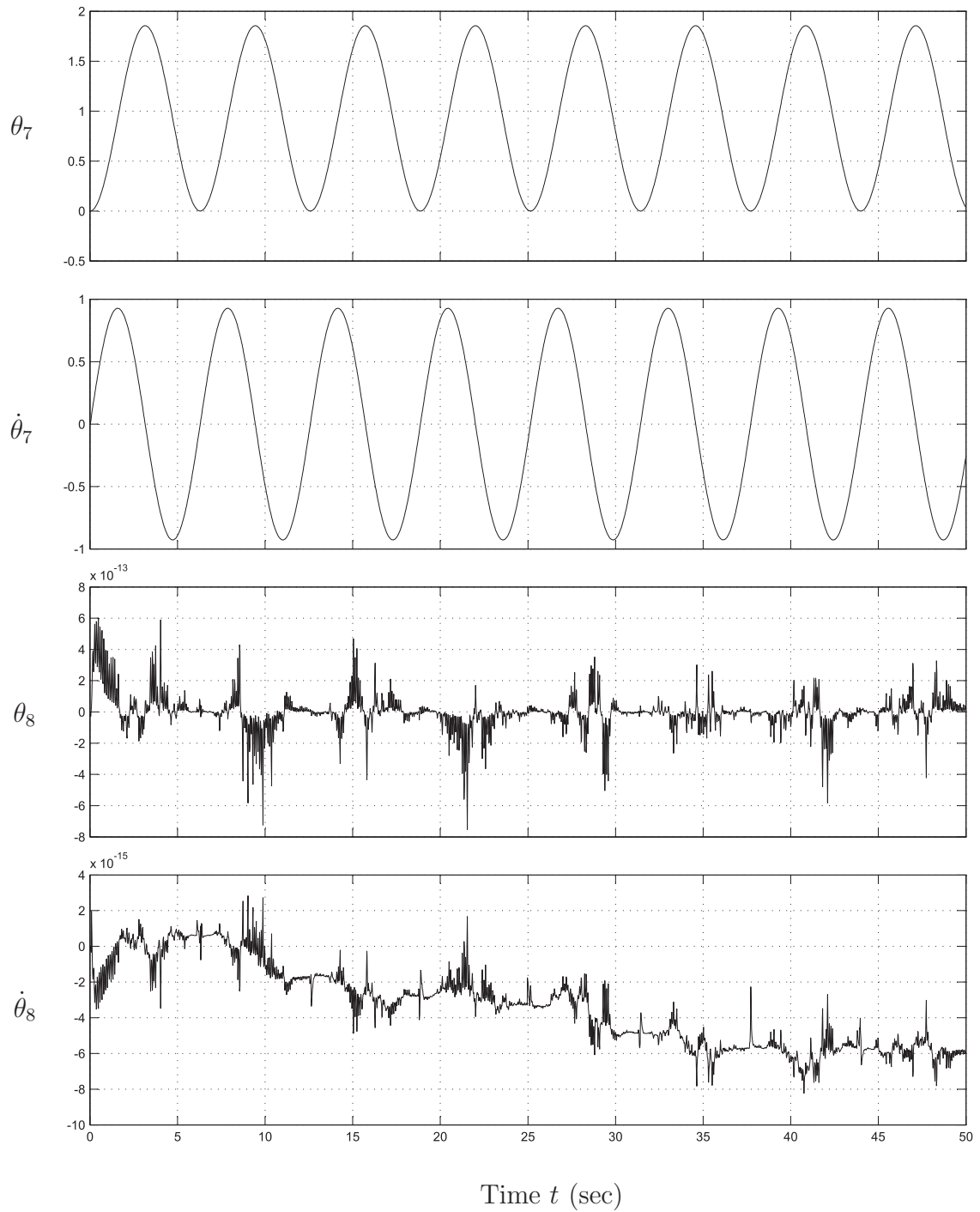


Figure 16: 1Hz (Same amplitude, phase difference 0°) output scope

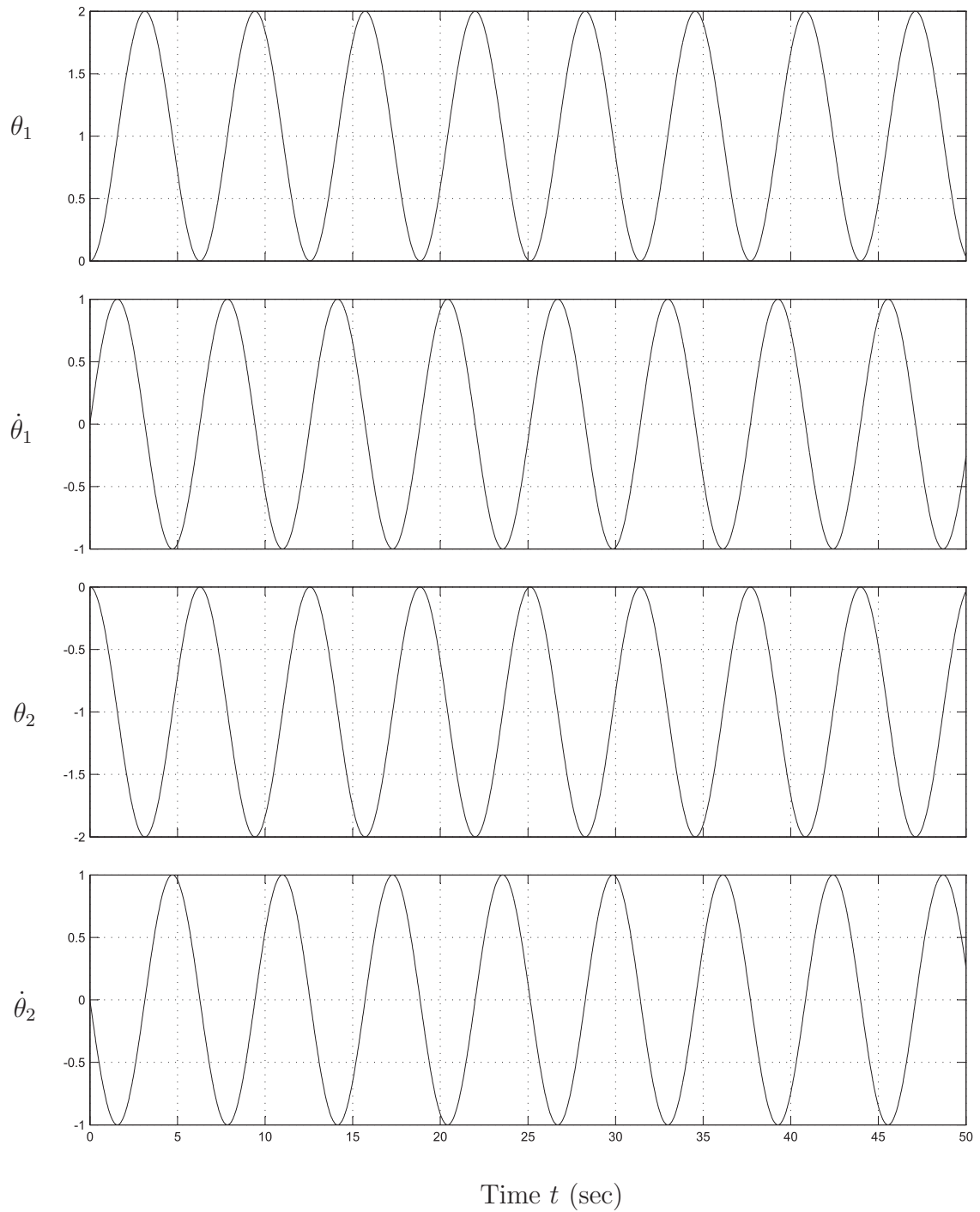


Figure 17: 1Hz (Same amplitude, phase difference 180°) input scope

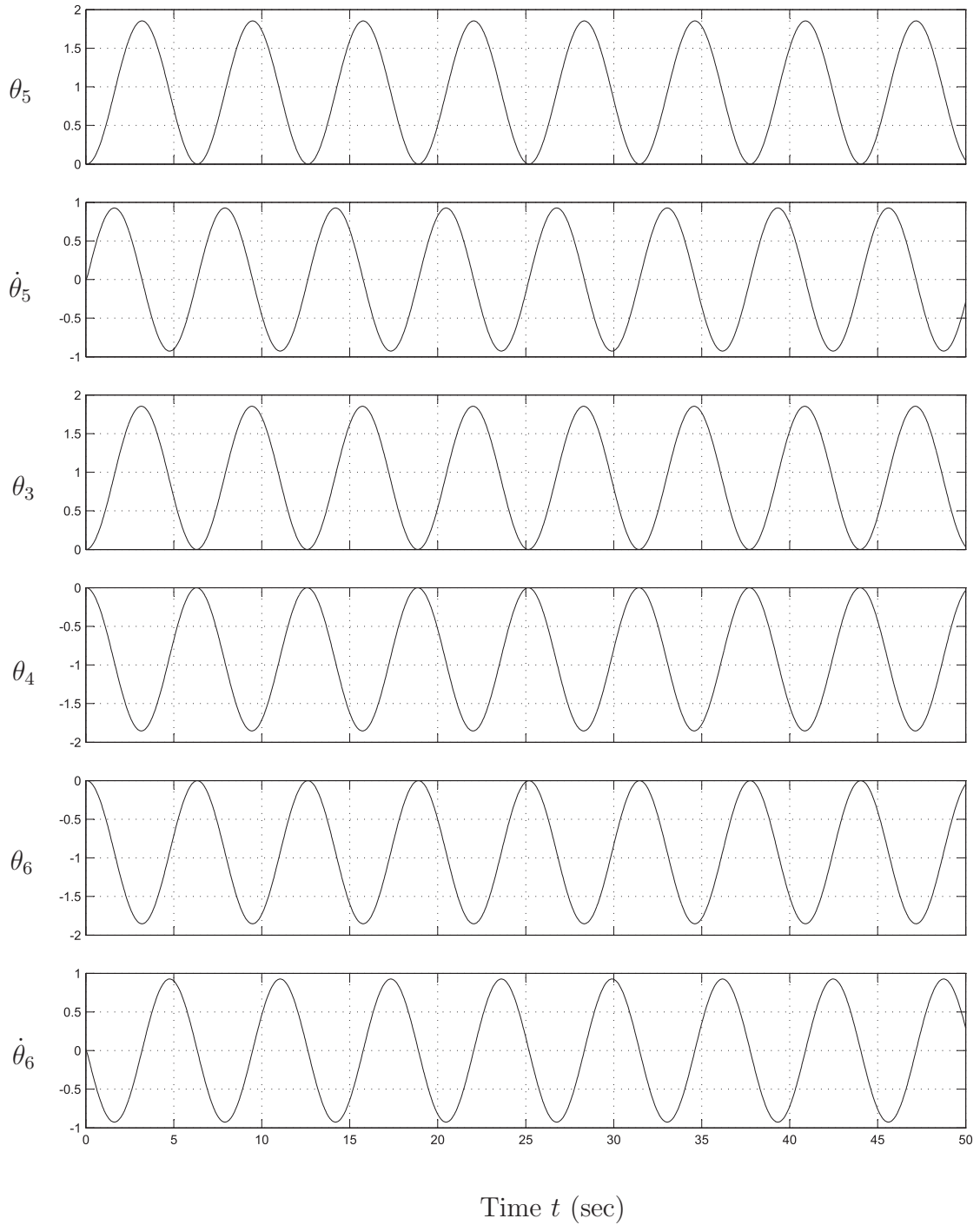


Figure 18: 1Hz (Same amplitude, phase difference 180°) state scope

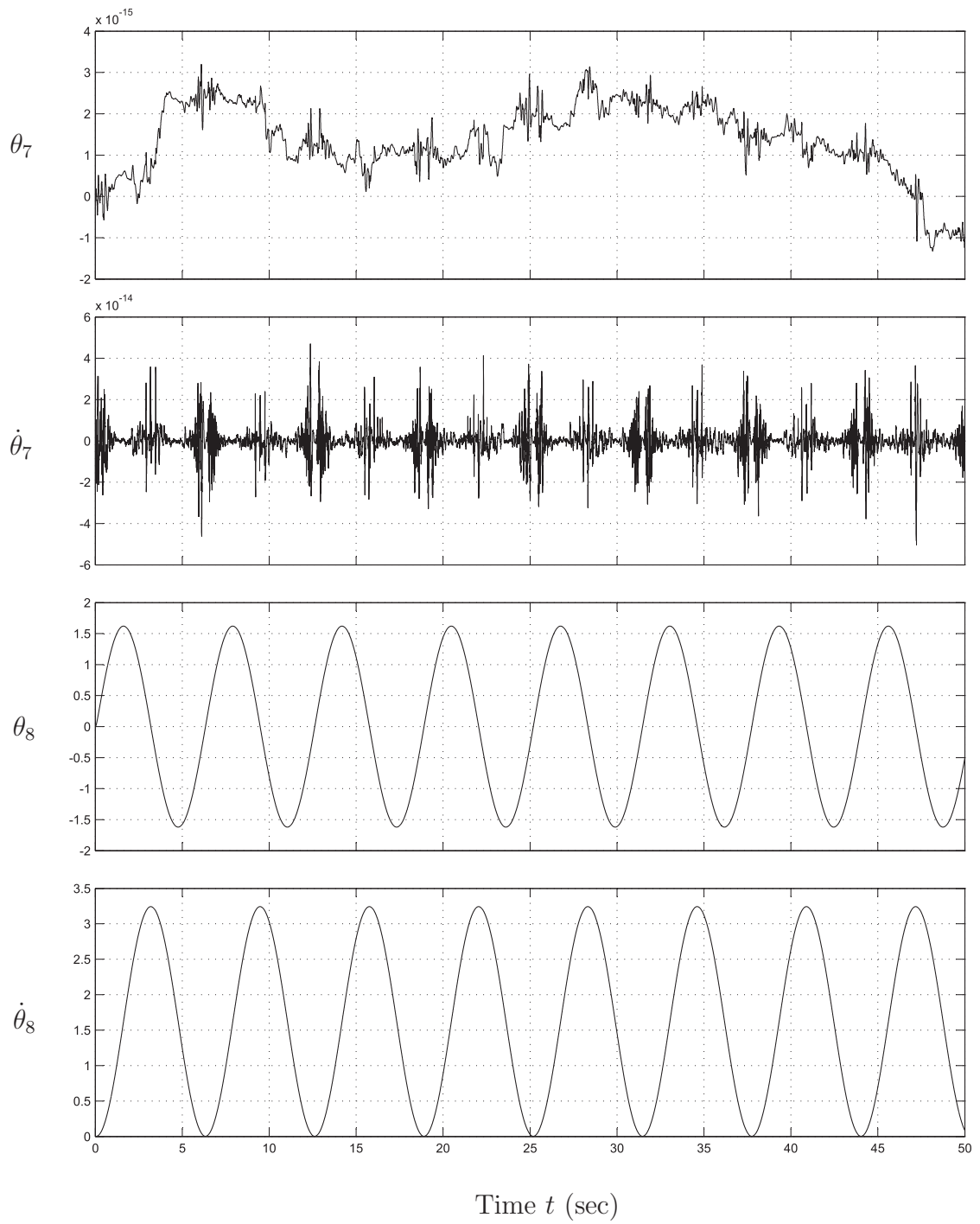


Figure 19: 1Hz (Same amplitude, phase difference 180°) output scope

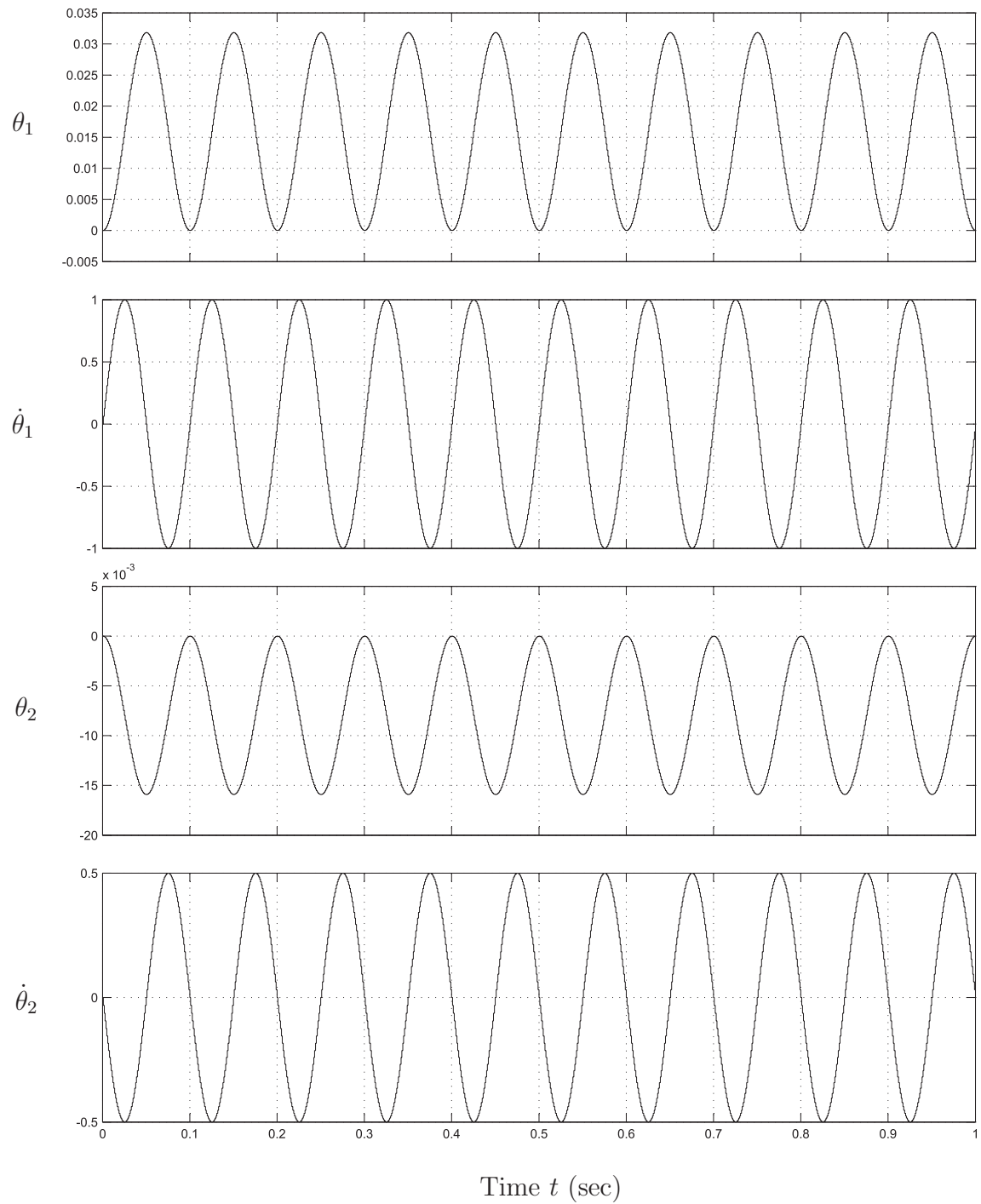


Figure 20: 10Hz (different amplitudes, phase difference 180°) input scope

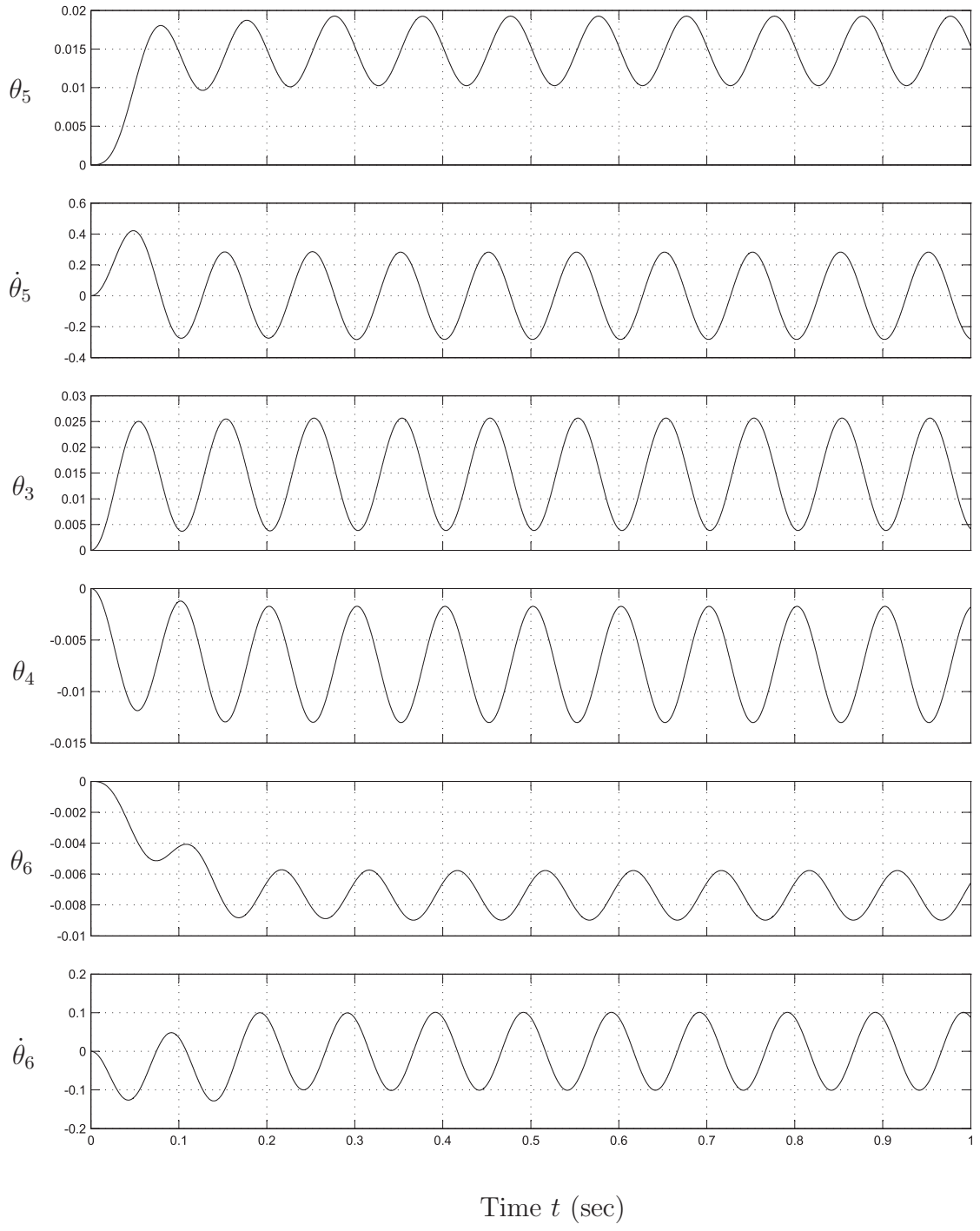


Figure 21: 10Hz (different amplitudes, phase difference 180°) state scope

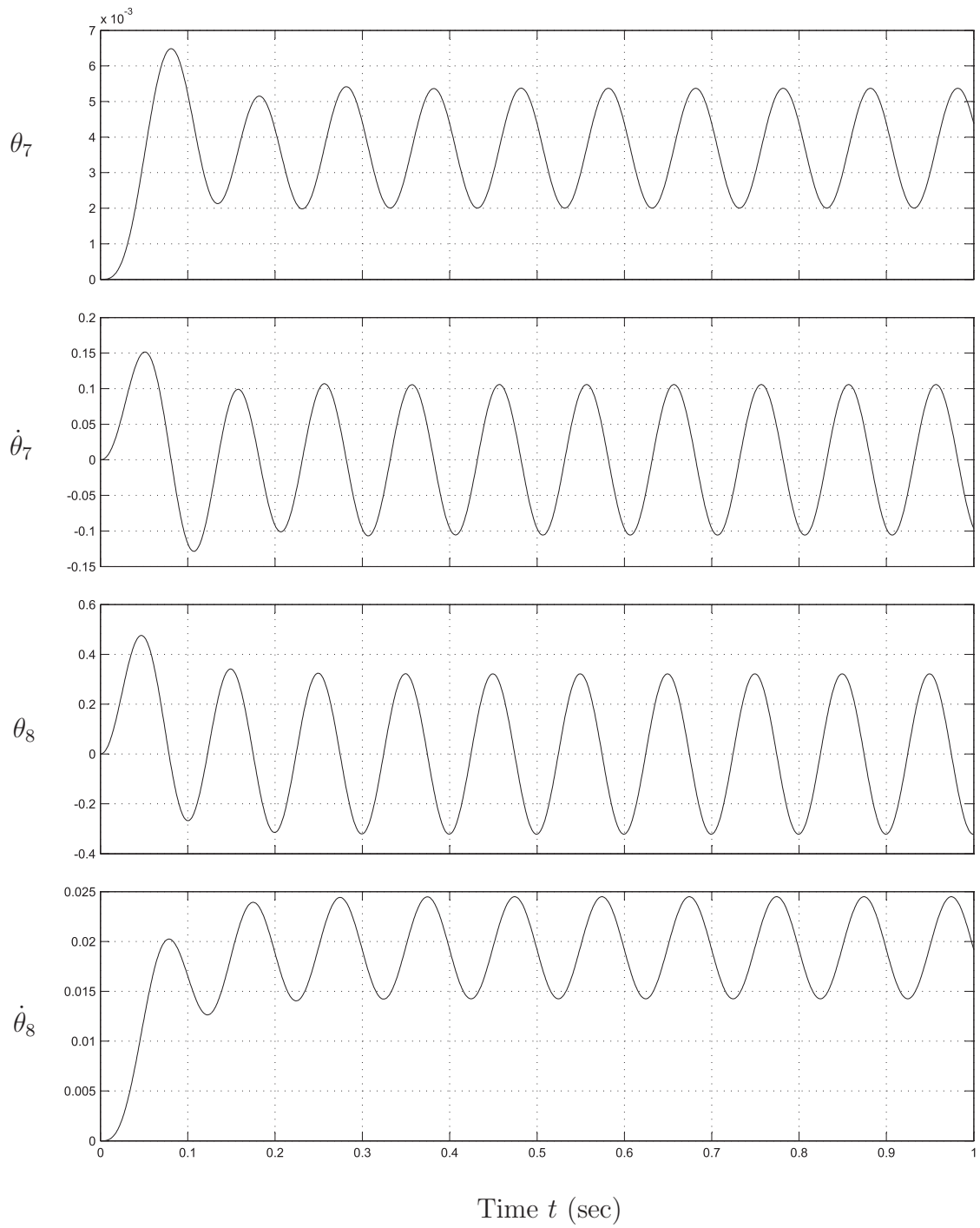


Figure 22: 10Hz (different amplitudes, phase difference 180°) output scope

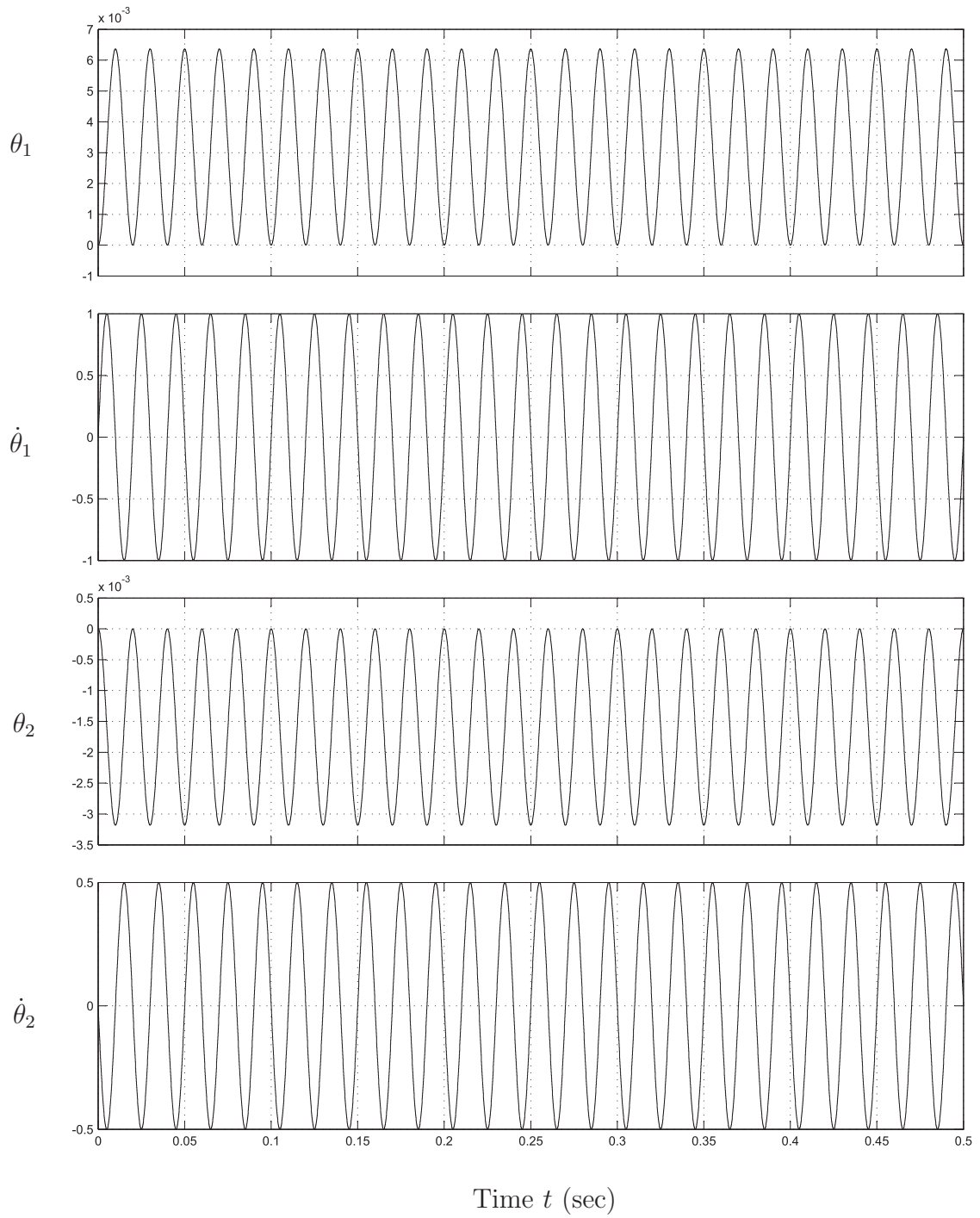


Figure 23: 50Hz (different amplitudes, phase difference 180°) input scope

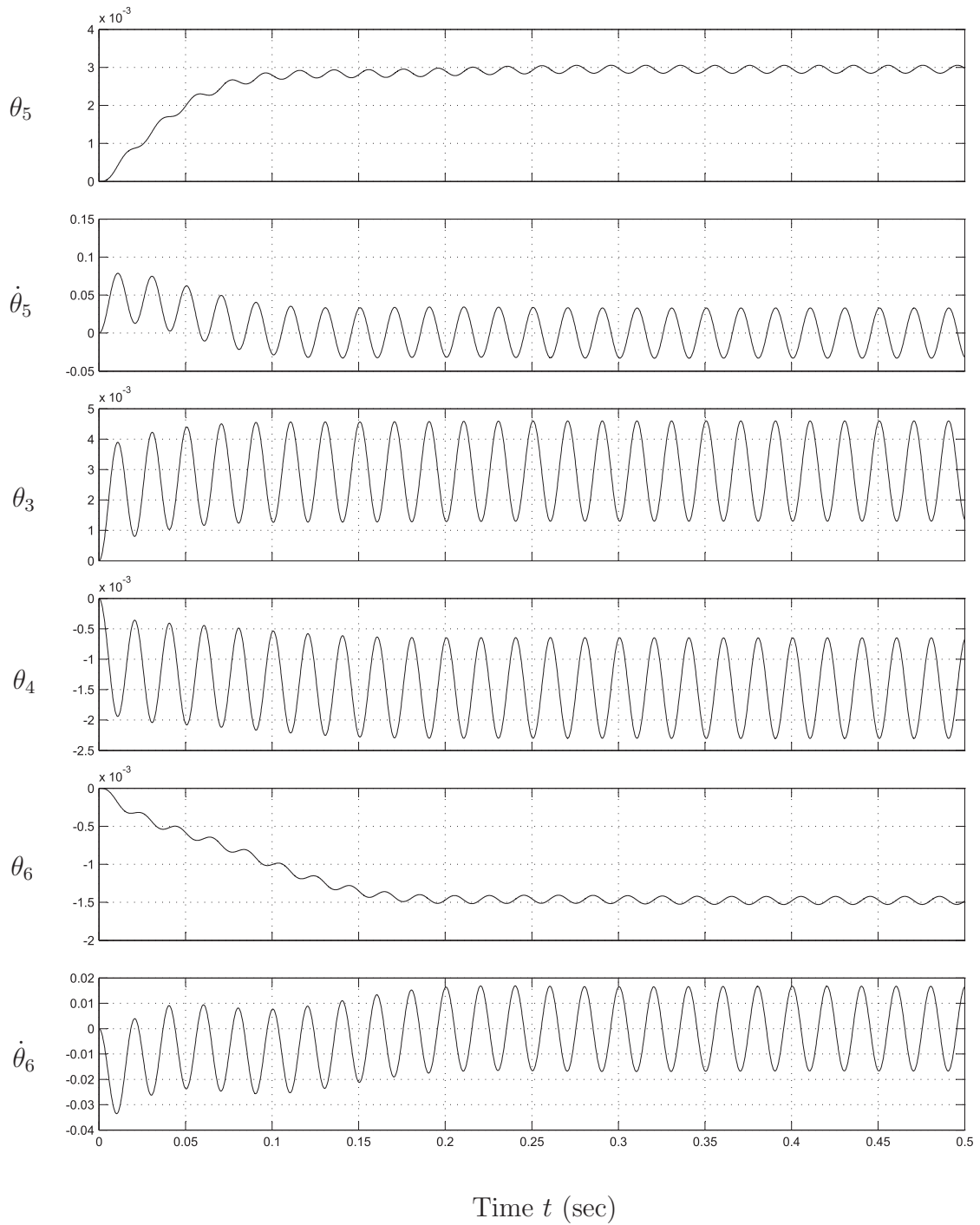


Figure 24: 50Hz (different amplitudes, phase difference 180°) state scope

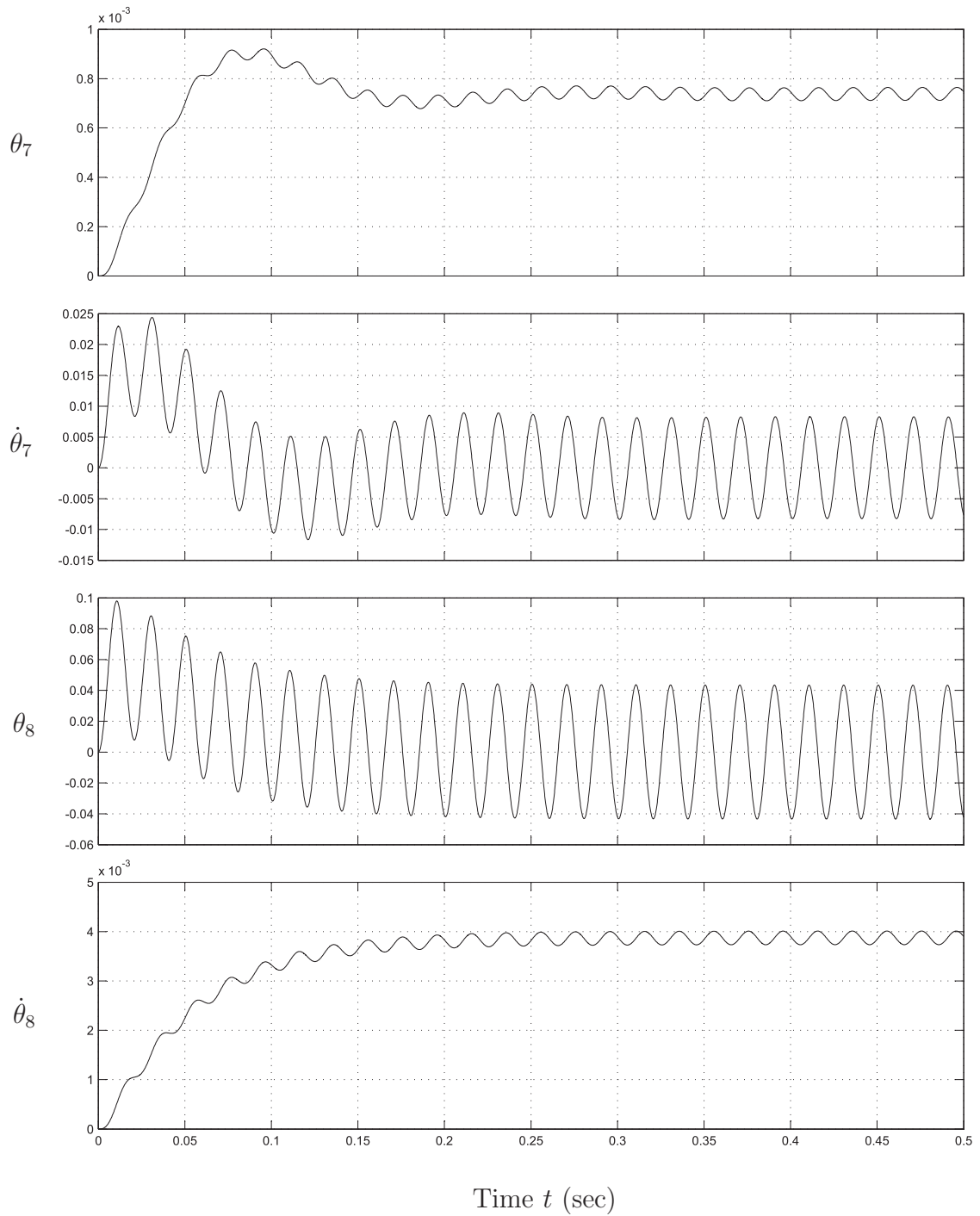


Figure 25: 50Hz (different amplitudes, phase difference 180°) output scope

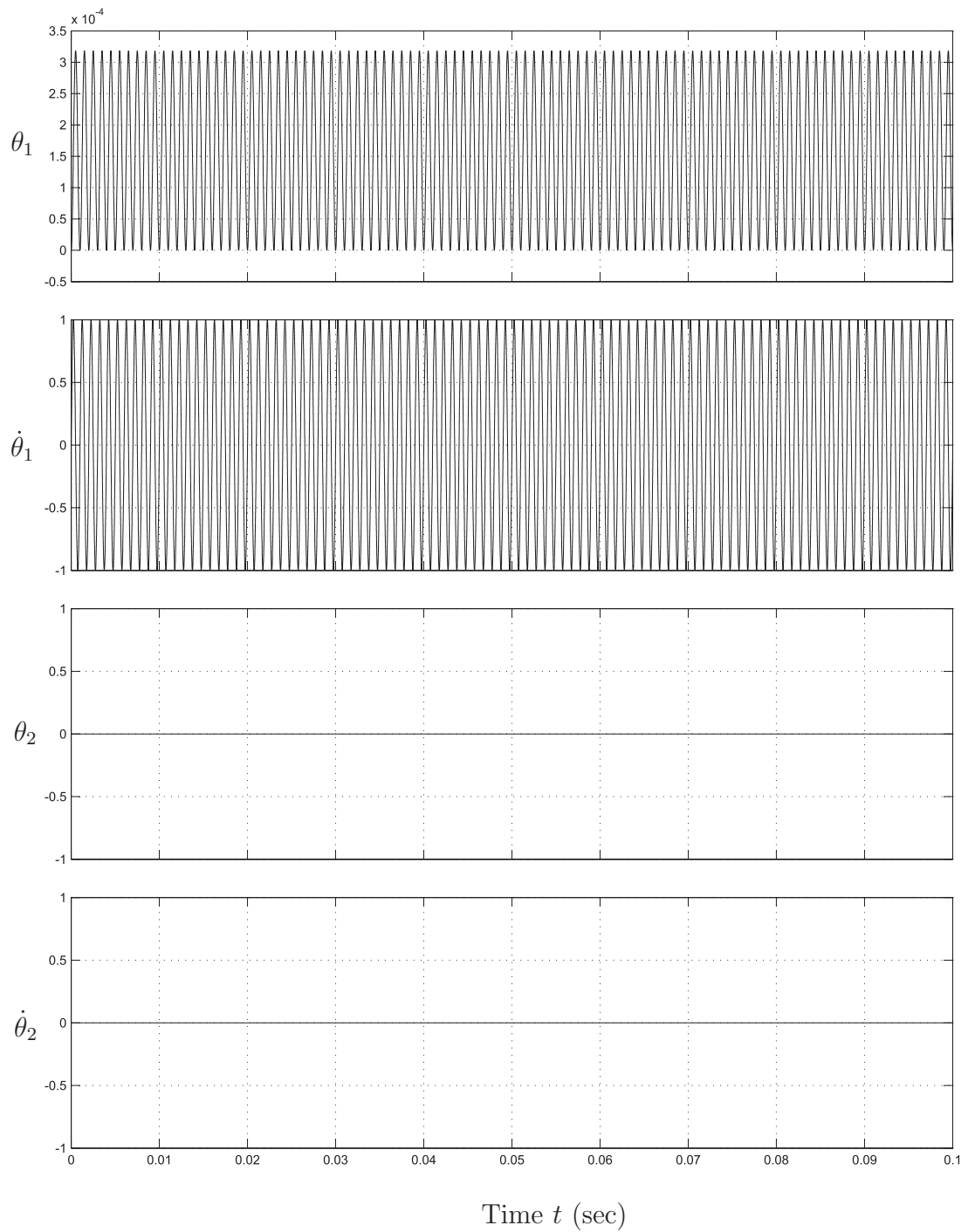


Figure 26: 1000Hz (different amplitudes, phase difference 180°) input scope

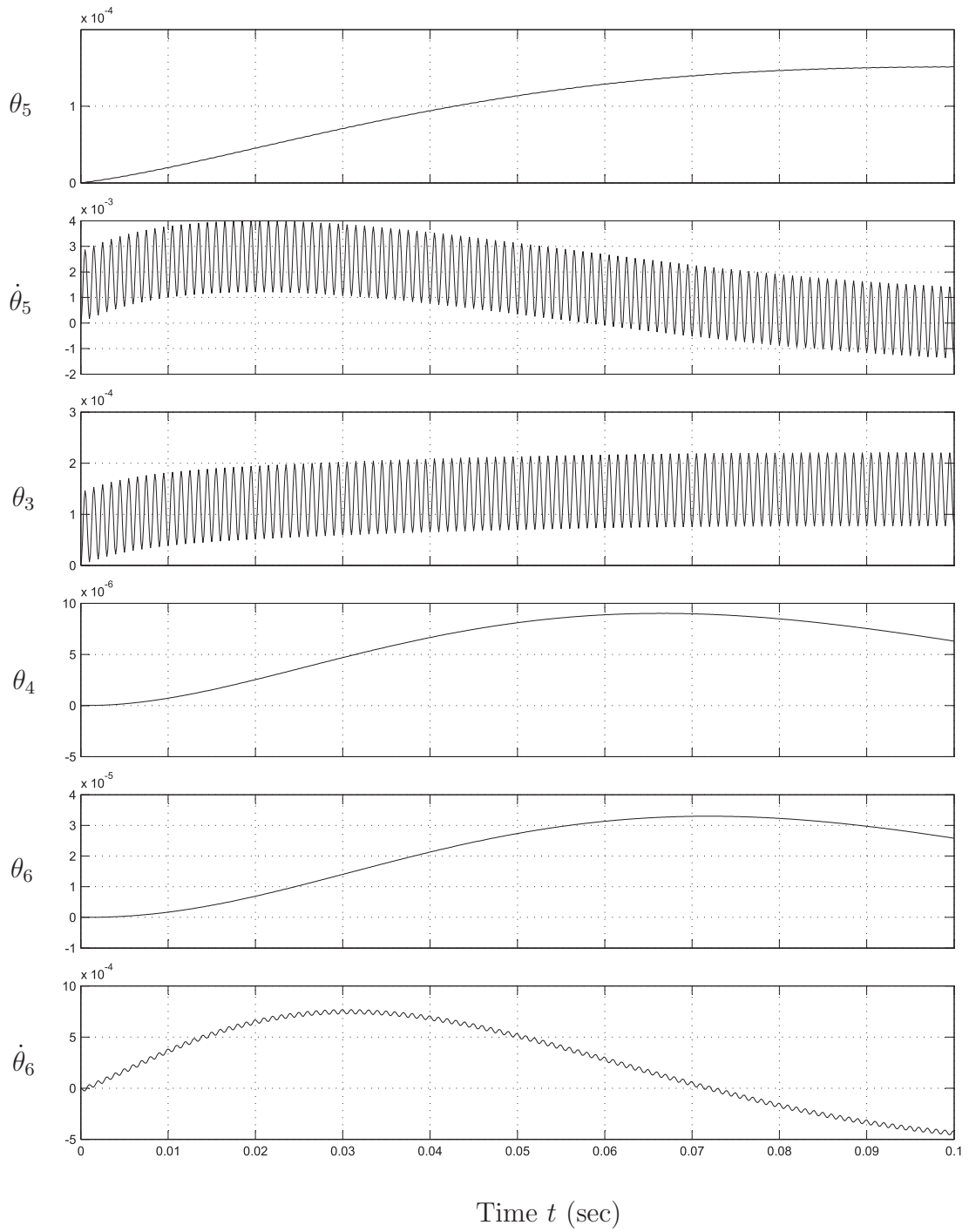


Figure 27: 1000Hz (different amplitudes, phase difference 180°) state scope

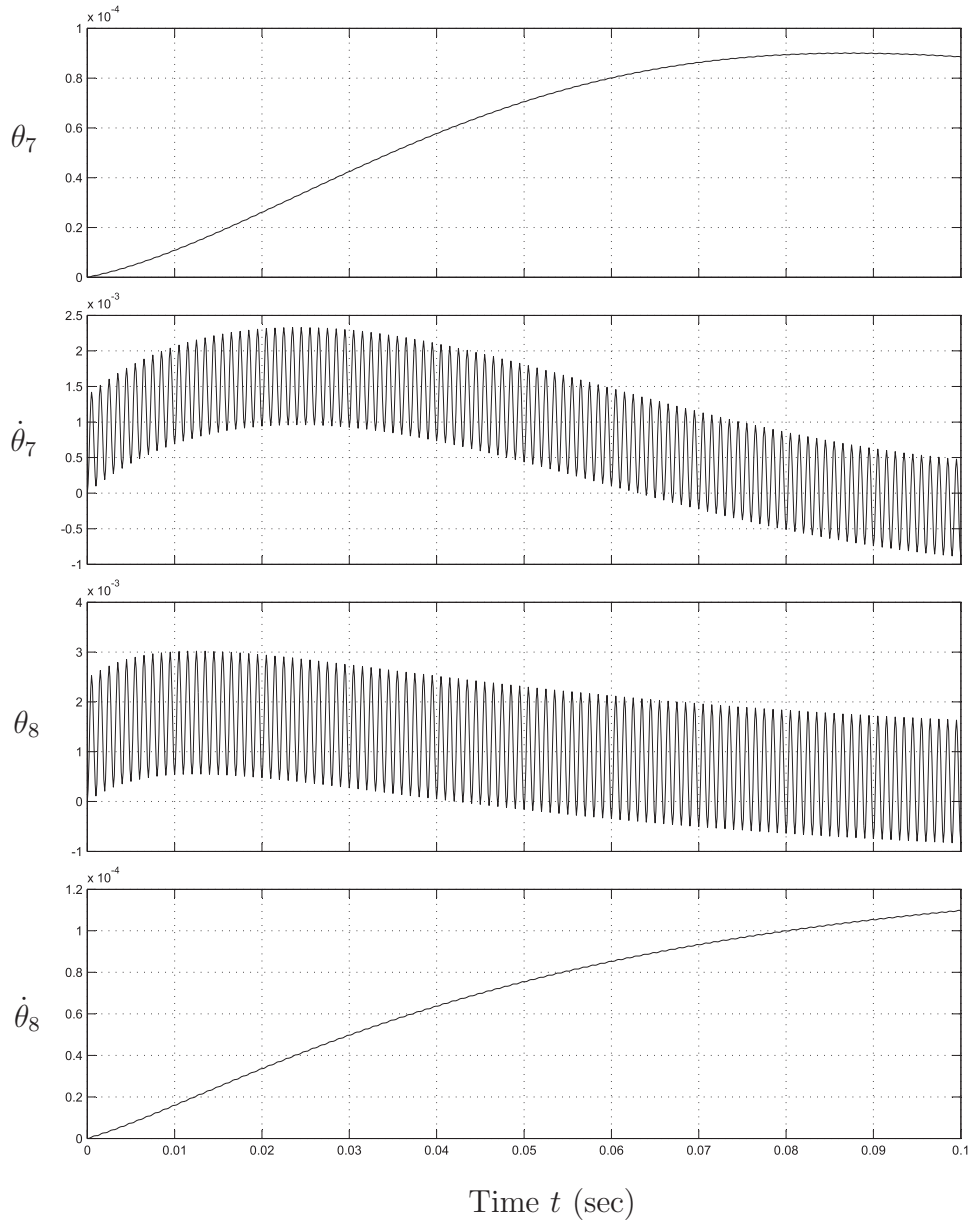


Figure 28: 1000Hz (different amplitudes, phase difference 180°) output scope

5.2 Controllability and Observability

Controllability and observability are concepts of system theory. Controllability refers to the ability to drive a system from one state to any other state. The controllability matrix $\mathbf{\Gamma}_c$ is given by

$$\mathbf{\Gamma}_c = [\mathbf{B} \ \mathbf{A}\mathbf{B} \ \mathbf{A}^2\mathbf{B} \ \dots \ \mathbf{A}^{n-1}\mathbf{B}] \quad (26)$$

where \mathbf{A} and \mathbf{B} are the state-space matrices appearing in eq.(17a). Using MATLAB, we calculate the controllability matrix and obtain its rank, namely, six, which means that the system is controllable. Observability refers to the ability to determine the state of a system from its inputs and outputs. The observability matrix $\mathbf{\Gamma}_o$, is given by

$$\mathbf{\Gamma}_o = [\mathbf{C} \ \mathbf{A}\mathbf{C} \ \mathbf{A}^2\mathbf{C} \ \dots \ \mathbf{A}^{n-1}\mathbf{C}]^T \quad (27)$$

where \mathbf{C} is the state-space matrix given by eq.(17b). Again, using MATLAB, we obtain the observability matrix, which also turns out to be of full rank, namely, six. Hence, we have a controllable and observable system.

6 Conclusions

We introduced here the design elements of a testbed for the Gearless Pitch-Roll Wrist. The various components involved in the testbed and the SECT are examined closely which is reported here. We developed the system model using a Lagrangian formulation and represented it in state-space form. The model transfer function was also derived, from which we were able to conclude that the system is both controllable and observable, and deemed, identifiable. A MATLAB Simulink system model was created and then simulation runs using harmonic inputs at 1Hz, 10Hz, 50Hz and 1000Hz were conducted. The allowable operation region, considering the limitations of the bearing within the SECT, was obtained.

The testbed is now ready to conduct experimental work on system identification. This

consists in estimating its stiffness and damping parameters using experimentally measured input-output data. To this end, the input-output data from measurements are to be analyzed and numerical results of the parameters are to be obtained. An experimental transfer function is to be developed and compared with the model transfer function.

References

- Angeles, J., 2008, *The Dynamics of Linear Mechanical Systems. An Introduction to Modelling, Analysis and Simulation*, Department of Mechanical Engineering and Centre for Intelligent Machines Technical Report, McGill University, Montreal
- Bai, S. P. and Angeles, J., 2005, “The design of a gearless pitch-roll wrist,” *Proc. 2005 IEEE International Conference on Robotics and Automation*, 18-22 April pp. 3213–3218
- Cannon, R. H., 1967, *Dynamics of Physical Systems*, McGraw-Hill Publishing Co., New York.
- Gosselin, C. M. and Caron, F., 1994. “The Agile Eye: a high-performance three-degree-of-freedom camera-orienting device”. *IEEE Int. Conf. on Robotics and Automation*, pp. 781–786.
- Hernandez, S., Bai, S., and Angeles, J., 2006. “The design of a Chain of spherical Stephenson mechanisms for a gearless robotic pitch-roll wrist”. *ASME J. Mech. Des.*, 128, pp. 422–429.
- Hsu, C. -H., Chang, C. -C., and Hsu, J. -J., 1999. “Structural synthesis of bevel-gear robotic wrist mechanisms”. *Proc. Natl. Sci. Counc. ROC(A)*, 23(4), pp. 518–525.
- Rosheim, M. E., 1989. *Robot Wrist Actuators*. Wiley, New York.
- Tsai, L. W., 1988. “The kinematics of spatial robotic bevel-gear trains”. *IEEE J. of Robotics and Automation*, 4(2), pp. 150–156.
- Song, X., 2002, *The Parameter Identification of a Novel Speed Reducer*, Master of Engineering Thesis, Department of Mechanical Engineering, McGill University, Montreal
- Wiitala, J. M. and Stanisic, M. M., 2000. “Design of an overconstrained and dextrous spherical wrist”. *ASME J. Mech. Des.*, 122, pp. 347–353.

A Commercial Components

A.1 Coupling Specification

D Series - Precision flexible shaft coupling for greater misalignment and axial motion.

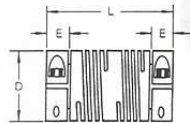
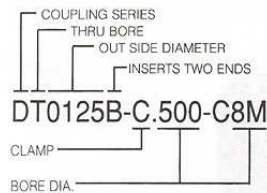
COUPLING FEATURES.

PHENOLIC INSERTS in each bore prevents heat and static electricity from damaging encoders, servo tachometers, resolvers and other rotary components.
 RESONANT FREQUENCY and WIND UP are minimized by the six short flexible beam design.
 CONSTANT VELOCITY - HIGH SPEED



NOTES:

1. EXAMPLE PART NUMBER



2. THRU BORE- The flexible beams have an inside relief to prevent the shafts from touching at the maximum misalignment.

3. CLAMPS are an integral part of the coupling and cannot be removed. When the screws are properly tightened, the clamp will hold to the torque rating of the coupling.

4. PEAK TORQUE is the maximum torque rating. The correct dynamic torque safety factor should be determined by the customer in accordance with the acceleration, deceleration, reversals and or sudden stop loads, etc.

5. TORQUE RATING is in pound inches, and WIND UP is in minutes per ounce inches and they are at maximum misalignment.

6. COUPLING MATERIAL IS 2024-T3.5 QQA225/6 ALUMINUM with MIL A8625 Type II black anodize.

7. INSERT INSULATORS are G10 glass filled phenolic and are available in the sized shown.

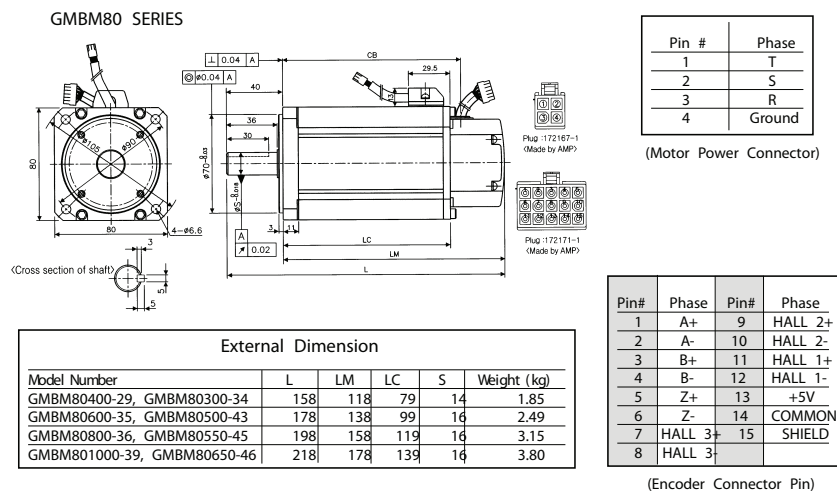
8. CAP SCREWS are hex socket, steel, black oxide finish.

9. CAUTION - REMOVE THE OIL FROM THE SHAFTS.

PART NUMBER (see note -1)	D DIA. +.000 -.010	L Length ±.020	E Bore Depth ±.010	MAXIMUM MISALIGNMENT			CLAMP SCREW (see notes 3 and 8)	PEAK TORQUE LB. IN. (see note 4)	WIND UP MIN./ OZ. IN. (see note 5)	STANDARD BORE SIZES (see note 7)	
				Angular	Parallel	Axial Motion				INCH	MM
DT0075A	.75	1.00	.230	5°	.020	.020	4-40	18	.85	.125 .156 .187 .250	4 5 6
DT0100A	1.00	1.50	.460	7°	.025	.040	6-32	45	.40	.187 .250 .312 .375	5 6 8 10
DT0125A	1.25	2.00	.600	10°	.035	.050	8-32	75	.26	.250 .312 .375 .437 .500	6 8 10 12
DT0150A	1.50	2.37	.700	15°	.045	.060	10-24	120	.26	.375 .437 .500 .625	10 12 14 15
DT0200A	1.97	3.00	.600	5°	.040	.060	1/4-20	245	.17	.375 .500 .625 .750 .875	

A.2 Servo Motor Specification

Brushless Servo Motors GMBM80 Series Mechanical Dimensions



Glentek, Inc.
208 Standard Street • El Segundo, California 90245 USA
(310) 322-3026 • (310) 322-7709 Fax • www.glentek.com

A.3 Torque Sensor Specification

FUTEK MODEL TRS605
Drawing Number: F11029-C
INCH [mm] R.O.= Rated Output

CONNECTOR CODE (CABLE PACKAGE WIRING CODE)			
GND (Shunt Cal)	Signal (Angle 1)	Signal (Torque)	GND (Torque)
PIN 'A' (YELLOW)	PIN 'B' (BLUE)	PIN 'C' (GREEN)	PIN 'D' (WHITE)
GND (Sensor Angle)	Power (Sensor)	Signal (Angle 2)	Power (Angle)
PIN 'E' (BLACK)	PIN 'F' (RED)	PIN 'G' (BROWN)	PIN 'H' (ORANGE)
N/C	Power (Shunt Cal)	N/C	Shield (Floating)
PIN 'J'	PIN 'K' (PURPLE)	PIN 'L'	PIN 'M'

NON CONTACT SHAFT TO SHAFT ROTARY TORQUE SENSOR W/ ENCODER
CE COMPLIANT

NOTE1 - ADDITIONAL M4 HOLE USED ON 20 & 50 Nm SENSORS

STOCK #	CAPACITY in-lb N m	Dia	A	B	C	E	F	G	H	I	J	K	L	N*	P*	Q	MAX AXIAL FORCE lb (N)	MAX RADIAL FORCE lb (N)
FSH02052	9 1															6	4.5 20	1 5
FSH02053	18 2	0.394	3.62	1.10	2.04	0.63	0.67	2.28	0.55	0.19	0.43	0.59	0.31				11 50	1 5
FSH02054	44 5	[10] g6	[92]	[28]	[52]	[16]	[17]	[58]	[14]	[5]	[11]	[15]	[8]				11 50	2 10
FSH02055	89 10																34 150	4.5 20
FSH02056	177 20	0.630	4.09	1.49	2.28	0.78	0.90	2.32	0.75	0.19	0.47	0.59	0.55	0.197	0.787	8	34 150	11 50
FSH02057	443 50	[16] g6	[104]	[38]	[58]	[20]	[23]	[59]	[19]	[5]	[12]	[15]	[14]	[5]	[20]		45 200	11 50

* Feather Keyways per DIN 6885
Keyways come pre-installed.

TORQUE SPECIFICATIONS:

RATED OUTPUT ±5VDC
 SAFE OVERLOAD 150% of R.O.
 ZERO BALANCE ±1% of R.O.
 EXCITATION (VDC) 11-26 VDC
 NONLINEARITY ±0.2% of R.O.
 HYSTERESIS ±0.1% of R.O.
 NONREPEATABILITY ±0.2% R.O.
 TEMP. SHIFT ZERO ±0.01% of R.O. / °F [±0.02% of R.O. / °C]
 TEMP. SHIFT SPAN ±0.01% of R.O. / °F [±0.02% of Load / °C]
 OPERATING TEMP. -13 to 176°F [-25 to +80°C]
 ROTATIONAL SPEED 7000 RPM MAX
 CONNECTOR: 12 pin Binder Series #581 (09-0331-90-12)

ACCESSORIES AND RELATED INSTRUMENTS AVAILABLE
 CALIBRATION (STD) Certificate of Conformance
 CALIBRATION (AVAILABLE) 5pt CW and CCW
 CALIBRATION TEST EXCITATION 12 VDC
 SHUNT CALIBRATION With sensor fully connected apply 11-26 VDC to Pins A & K to generate 5VDC nom output.

ENCODER SPECIFICATIONS:

OUTPUT IMPULSE (TTL)
 PULSES / REV 2 x 360
 EXCITATION 5 VDC
 ANGLE 1- LEADING PULSE
 ANGLE 2- TRAILING PULSE (90°)


FUTEK
 ADVANCED SENSOR TECHNOLOGY, INC.

This drawing is submitted solely for the information and exclusive use of the original addressee. It is not to be divulged in whole or in part, by any firm or individual without written permission from FUTEK

10 THOMAS
 IRVINE, CA 92618 USA
 1-800-23-FUTEK (38835)



INTERNET:
<http://www.futek.com>

A.4 Control Board Specification



QUANSER
INNOVATE. EDUCATE.

Specification and Features

CONTROL SOLUTIONS

Q8 High-Performance H.I.L. Control Board

Product Information Sheet C1 - 2 - rev. B

GENERAL	
Interface	PCI
PCI Bus Width	32-bit
Bus Speed	33 MHz
ANALOG INPUTS	
Channels	8 SE
Resolution	14-bit
Input Range (fixed)	± 10V
Conversion Time & Sampling Frequency*	
1 or 2 channels simultaneous	1.2 µs / 192 kHz
All 8 channels simultaneous	17.8 µs / 56 kHz
*The values above are measurements of the computation time of the I/O specified. On-board hardware FIFO allows A/D conversions to be performed in the background by the hardware, thus permitting control calculations and A/D to be overlapped.	
Features	
Simultaneous Sample & Hold	
ANALOG OUTPUTS	
Channels	8
Resolution	12-bit
Slew Rate	2.5 V / µs
Output range:	
Bipolar:	± 5V, ± 10V
Unipolar:	0-10V
Conversion Time **	
1 channel	0.62 µs
2 channels simultaneous	0.62 µs
8 channels simultaneous	1.35 µs
**The values above are measurements of time to write to the D/A. On-board double-buffering allows D/A conversions to be performed in the background by the hardware, thus permitting control calculations and D/A to be overlapped.	
Features	
Individual mode and gain selectability	
Known state on power-up or reset	
Simultaneous output	
ENCODER INPUT COUNTERS	
Quadrature Encoder Inputs supported	4
Counter size	24-bit
Max. A and B Frequency in Quadrature	2 MHz
Max. Count Frequency in 4X Quadrature	8 MHz
Max. Count Frequency in Non-quadrature	15 MHz
Conversion Time	
Single Encoder Read	0.50 µs
4 Simultaneous Encoder Reads	2.50 µs
All 8 channels simultaneous	4.72 µs
Features	
Simultaneous Sampling	
Single-Ended Inputs	
Non-quadrature (count/direction) and 1X, 2X or 4X quadrature modes	
Extensive Index Pulse Signal Support	
individually programmable count and index modes, and filter clocks	
TTL/CMOS compatible	

DIGITAL I/O	
Number of lines	32
Conversion Time	
Single Digital Output	0.18 µs
Multiple Digital Output (32 lines)	0.18 µs
Single Digital Input	0.68 µs
Multiple Digital Input (32 lines)	0.79 µs
Features	
Totem-pole outputs	
Known state on power-up or reset	
Individually Software Programmable	
Single access read/write of all channels	
GENERAL PURPOSE COUNTER-TIMERS	
Number of counter-timers	2
Counter-Timer Size	32-bit
Timer Resolution	30 ns
Features	
Configurable as PWM Outputs	
One Counter Configurable as Watchdog Timer	
One Counter Allows Hardware Gating	
Software enabling/disabling	
WATCHDOG TIMERS (reconfigured GP Counter-Timers)	
User programmable Watchdog Timers	1
Features	
Software enabling/disabling	
Automatic reset of Analog Outputs & Digital I/O	
PWM OUTPUTS (reconfigured GP Counter-Timers)	
User-programmable PWM outputs	1
EXTRA FEATURES	
Fused Encoder Section with LED status	
Fuse monitoring with watchdog and interrupt capability	
55 configurable interrupt sources	
External A/D Triggering Support	
SOFTWARE SUPPORT	
Real-Time Target Support ***	
Quanser WinCon	
The Mathworks xPC Target	
OPAL-RT RT-LAB	
National Instruments LabVIEW RTX	
*** Software support provided by their respective vendors.	
OS Drivers	
Windows 2000, XP	
Ardence RTX	
API	
C	
C++	
ActiveX	
.NET (VB, C#, C++ and others)	
LabVIEW, LabVIEW RTX	
MATLAB	
MATRIXx	



With Quanser the possibilities are infinite

+1 (905) 940-3575 www.quanser.com

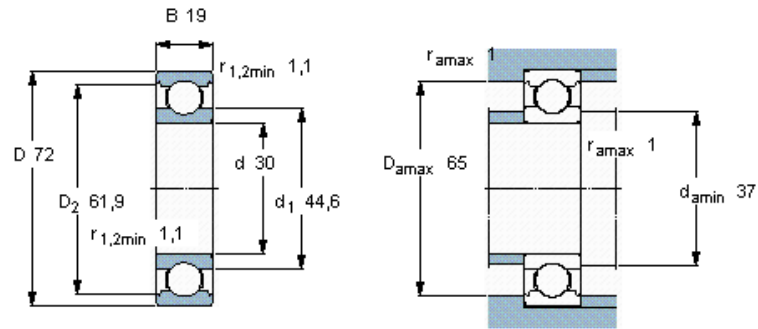
Products and/or services referred to herein are trademarks or registered trademarks of Quanser Inc. and/or its affiliates. Other names mentioned herein are trademarks or registered trademarks of their respective owners. © 2006 Quanser Inc. All rights reserved. Specifications are subject to change without notice. Errors and omissions excepted.

A.5 SECT Deep groove ball bearings SKF-6306

Deep groove ball bearings, single row, unsealed

Principal dimensions			Basic load ratings		Fatigue load limit P_u	Speed ratings		Mass	Designation
d	D	B	dynamic	static		Reference speed	Limiting speed		
mm			kN		kN	r/min		kg	-
30	72	19	29,6	16	0,67	20000	13000	0,35	6306 *

52



Calculation factors

k_r 0,03
 f_0 13

B Detailed Drawings

Attached to the end of each subsection are the detailed technical drawings.

B.1 Motor Supports

The motor housing, shown in Fig. 29, needs to firmly hold the motor on the testbed base platform. One of the essential aspects of the design was to ensure that the axes of the servomotor shafts are aligned with those of the SECT input shafts. Moreover, a single monolithic structure provides robustness and is more accurate to fabricate. The foregoing design consists of only two parts, namely, the motor support and a flat plate to attach the servomotor to the support. The machining of the motor housing was completed by the Machine Tool Laboratory of the McGill Department of Mechanical Engineering. Shown in Fig. 30 is the completed motor housing along with the Glentek servomotors.

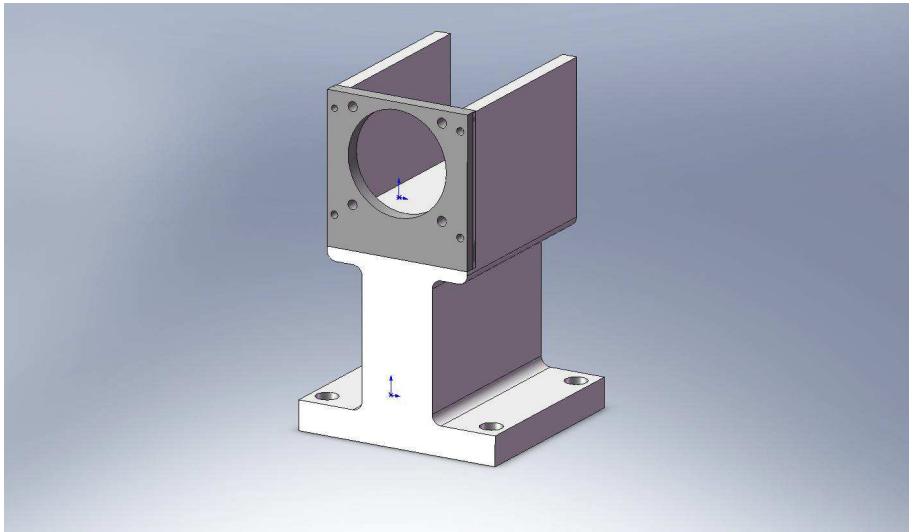


Figure 29: Servo Motor Support CAD model

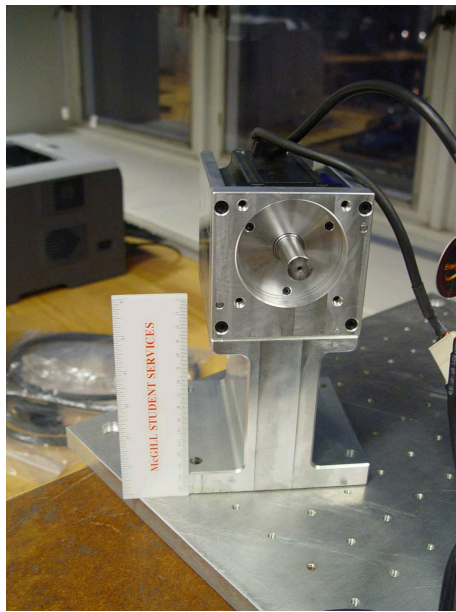


Figure 30: Housing of the Servo Motor

B.2 Torque Sensor Supports

Similar to the design requirements of the motor housing, the Torque sensor supports were fabricated. Here, too, we use a single monolithic structure and assign equal importance to the alignment of the torque sensor shafts with the SECT input shafts as that assigned to the alignment of servomotor shaft with SECT shaft axes. The support, as shown in Fig. 31, has been machined by the McGill Machine Tool Laboratory.



Figure 31: Torque Sensor Supports

B.3 Dummy Gripper

We designed a dummy gripper in order to provide a load to the PRW. The dummy gripper weight is preselected to be of 4.91N (0.5 kg) approximately, and will be replaced by a functional gripper at a later stage. Fig. 32 illustrates the placement of a counter-weight. A simple calculation using static analysis is carried out to determine the counter-weight, to be placed diametrically opposite to the dummy gripper, on the central ring. The distances from the centre of the ring, O , to the mass centre of the gripper, G , and to the mass centre of the counter-weight, C , are constant; and given by e and d respectively.

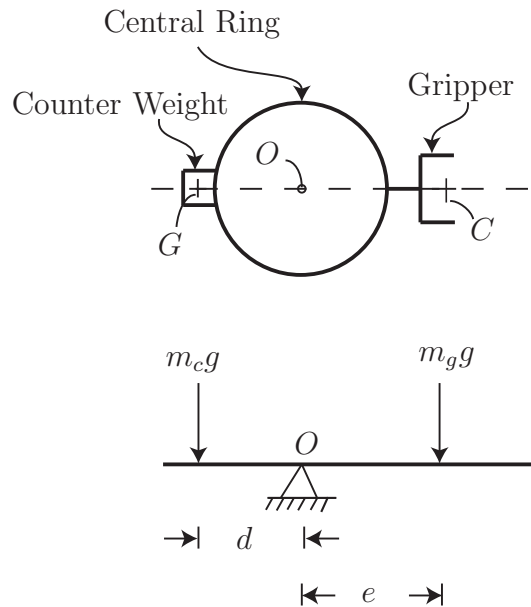


Figure 32: Dummy Gripper and Counter-weight balancing on the SECT

With an approximate weight dimension, the dummy gripper and counter-weight, shown in Fig. 33, are modelled in Pro/ENGINEER. Mass properties were calculated in Pro/ENGINEER, which showed that the centre of mass of the ring-cam-shaft-gripper-counter-weight composite body, lies extremely close to the centre O of the central ring of the SECT. Notice that the counter-weight is made of two brackets held together using a pair of screws and nuts. The counter-weight is also to be held in position on the central ring using screws.

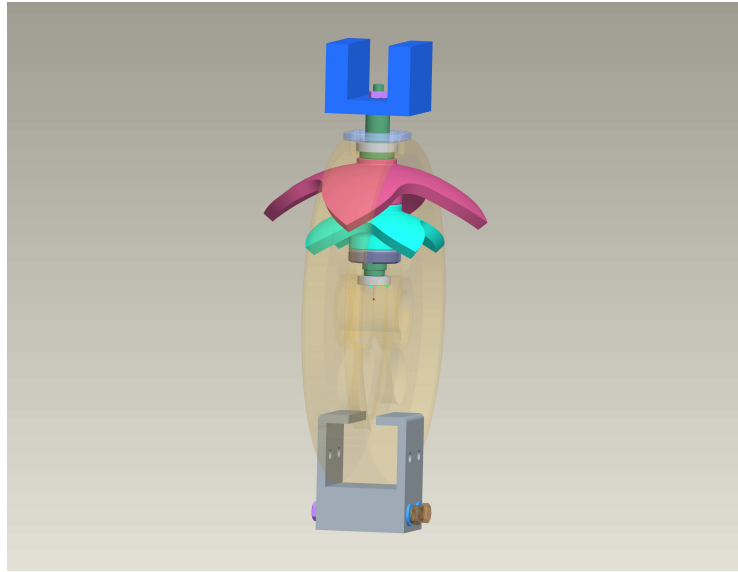


Figure 33: SECT ring-cam-shaft-gripper-counterweight composite CAD model

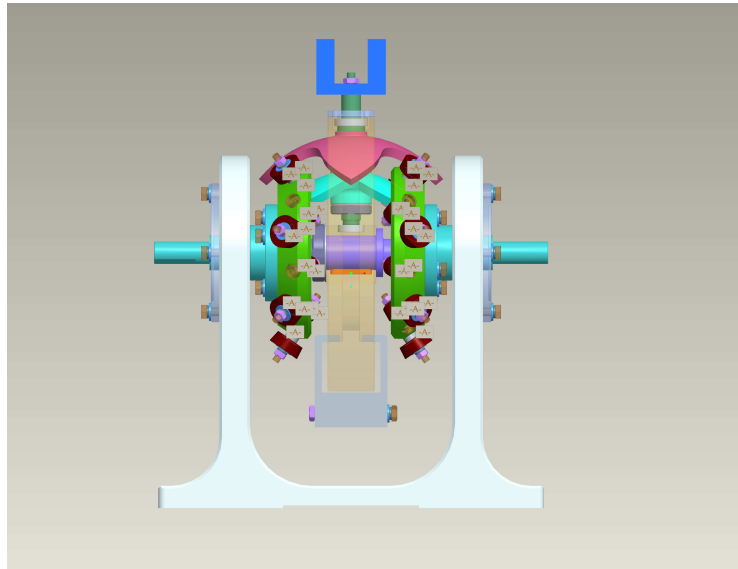


Figure 34: SECT with dummy gripper and counter-weight CAD model Front View

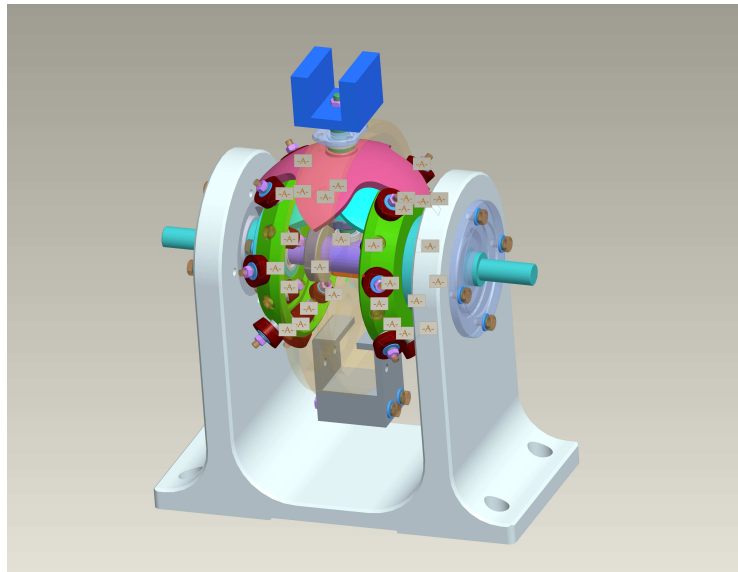


Figure 35: SECT with dummy gripper and counter-weight CAD model Isometric View

C Simulation

C.1 Sample M-file for the Simulink Model

```
% System Parameters
J2=3.8681291e-3; % units - kg*m^2
J3=1.2750004e-2; H3=4.2363841e-2;
c1=7.83e-3/(pi/180); %units N*s/rad
c2=8.35e-3/(pi/180);
c3=c1*(1-0.15); % +/- 10%-20%
% c3=c1*(1+0.15);
k1=2.11/(pi/180); % units N*m/rad
k2=0.76/(pi/180); N=7; M=4; M33=J2+(H3/4)+(J3*N^2/(4*M^2));
M34=(H3/4)-(J3*N^2/(4*M^2)); M44=J2+(H3/4)+(J3*N^2/(4*M^2));
M43=(H3/4)-(J3*N^2/(4*M^2)); C33=c2+(c3/4)+(c3*N^2/(4*M^2));
C34=(c3/4)-(c3*N^2/(4*M^2)); C43=(c3/4)-(c3*N^2/(4*M^2));
C44=c2+(c3/4)+(c3*N^2/(4*M^2));

%Input Signal
theta1_dot_amp=1;
theta1_dot_fre=100*pi;%100*pi
theta1_dot_pha=0; theta2_dot_amp=-1/2; theta2_dot_fre=100*pi;
theta2_dot_pha=0;

%Simulation Parameters
ENDTIME=1; %Simulation time 1 second
sim('modelPWR20081105') %Figure 13 Simulink flow Model
plot(t,dotth1) %Scope Result
```